

Testing the relativistic precession model using low frequency and kHz quasi-periodic oscillations in neutron star low mass X-ray binaries with known spin

Marieke van Doesburgh,^{1*} Michiel van der Klis¹

¹*Anton Pannekoek Institute, University of Amsterdam, Science Park 904, Postbus 94249, 1090 GE Amsterdam, The Netherlands*

Accepted 2016 November 11. Received 2016 October 19; in original form 2016 August 5

ABSTRACT

We analyze all available RXTE data on a sample of 13 low mass X-ray binaries with known neutron star spin that are not persistent pulsars. We carefully measure the correlations between the centroid frequencies of the quasi-periodic oscillations (QPOs). We compare these correlations to the prediction of the relativistic precession model (RPM) that, due to frame dragging, a QPO will occur at the Lense-Thirring precession frequency ν_{LT} of a test particle orbit whose orbital frequency is the upper kHz QPO frequency ν_u . Contrary to the most prominent previous studies, we find two different oscillations in the range predicted for ν_{LT} that are simultaneously present over a wide range of ν_u . Additionally, one of the low frequency noise components evolves into a (third) QPO in the ν_{LT} range when ν_u exceeds 600 Hz. The frequencies of these QPOs all correlate to ν_u following power laws with indices between 0.4–3.3, significantly exceeding the predicted value of 2.0 in 80% of the cases (at 3 to $>20\sigma$). Also, there is no evidence that the neutron star spin frequency affects any of these three QPO frequencies as would be expected for frame dragging. Finally, the observed QPO frequencies tend to be higher than the ν_{LT} predicted for reasonable neutron star specific moment of inertia. In the light of recent successes of precession models in black holes, we briefly discuss ways in which such precession can occur in neutron stars at frequencies different from test particle values and consistent with those observed. A precessing torus geometry and other torques than frame dragging may allow precession to produce the observed frequency correlations, but can only explain one of the three QPOs in the ν_{LT} range.

Key words: X-rays: binaries – accretion, accretion disks – stars: neutron – binaries: close

1 INTRODUCTION

General Relativity predicts that frame dragging causes nodal precession of misaligned orbits around spinning objects. Quasi periodic oscillations (QPOs) in the Fourier power spectra of neutron star low mass X-ray binaries (NS-LMXBs, see van der Klis 2006 for a review) have been linked to orbital motion in the inner accretion disk. Closest to the neutron star Keplerian orbital frequencies of ~ 1 kHz are expected, and QPO pairs of this frequency are widely found. The behaviour of kHz QPOs is well studied as they are thought to provide an excellent opportunity to test GR in the strong field regime. Their frequencies vary with time, and correlate with those of QPOs at much lower frequency (< 80 Hz) (Ford & van der Klis 1998; Psaltis et al. 1999). The rela-

tivistic precession model (RPM) of Stella & Vietri (1998) explains the QPOs at frequencies of a few tens of Hz as being due to nodal precession of the orbits at the inner edge of the disk whose orbital frequency is identified with the frequency of the upper (highest frequency) kHz QPO. The predicted QPO frequency is once or twice (due to twofold symmetry existing in the tilted accretion disk geometry) the Lense-Thirring precession frequency of a test particle

$$\nu_{LT} = \frac{8\pi^2 I \nu_K^2 \nu_s}{c^2 M} = 13.2 I_{45} m^{-1} \nu_{K,3}^2 \nu_{s,2.5} \text{ Hz}, \quad (1)$$

where $M = m \cdot M_\odot$ and $I = 10^{45} I_{45} \text{ g cm}^2$ are the neutron star mass and moment of inertia, respectively, $\nu_K = 10^3 \nu_{K,3}$ Hz is the Keplerian orbital frequency, and $\nu_s = 300 \nu_{s,2.5}$ Hz the neutron star spin frequency: the frequency of the low frequency QPO is predicted to be proportional to the spin frequency and quadratically related to the upper kHz QPO

* E-mail: m.j.vandoesburgh@uva.nl

frequency. For realistic equations of state I_{45}/m ranges from 0.5 to 2 (Friedman et al. 1986).

In a study of the QPOs in three LMXBs with neutron stars of uncertain spin this quadratic dependence was confirmed by van Straaten et al. (2003) to remarkable precision. The authors reported a best-fit power law index of 2.01 ± 0.02 . In the past decade many LMXB neutron star spin frequencies have been measured using pulsations and burst oscillations (see Patruno & Watts 2012 for a review). It was found that the three sources studied by van Straaten et al. (2003) have quite different spin frequencies, raising the issue as to why their QPO frequency correlations coincide (van der Klis 2006).

Black hole LMXBs show similar low-frequency (< 80 Hz) QPOs to NS-LMXBs (Wijnands & van der Klis 1999; Klein-Wolt & van der Klis 2008) and they may follow similar frequency correlations (Psaltis et al. 1999). Also, a set of three simultaneous QPO frequencies showing a remarkable match to the RPM prediction for the orbital, periastron and Lense-Thirring frequencies was reported in the BH binary GRO J1655–40 by Motta et al. (2014). Currently, the model best explaining the X-ray spectral variations with black hole Type C QPO frequency involves solid-body Lense-Thirring precession of a hot inner flow (Ingram et al. 2009). In BH-LMXBs, the spin is a free parameter. As in NS-LMXBs we can measure the spin frequency directly, and contrary to high-frequency QPOs in BH, NS kHz QPOs are observed to vary over a wide range of frequencies, we can further constrain the precession model by studying the QPOs in these systems.

With this motivation, we undertook to test the relativistic precession model in the entire sample of neutron star sources in the (now complete) RXTE archive for which the spin frequency is known and that show the relevant QPOs. These conditions are met by burst oscillation sources and by accreting millisecond X-ray pulsars (AMXPs).

For the AMXPs, van Straaten et al. (2005) found that the correlations between QPO frequencies are offset from one another and from those observed in non-pulsating LMXBs by varying factors. They found that a shift in kHz QPO frequency was the simplest explanation for the offsets, but a clear physical origin could not be identified. Recently, Bult & van der Klis (2015a) showed that the pulse amplitude of pulsar SAX J1808.4–3658 differs markedly depending on whether the kHz QPO frequency is higher or lower than the spin frequency of the neutron star; a strong indication that the accretion flow is affected by the magnetic field. Additionally, Altamirano et al. (2012) show for the 11 Hz pulsar IGR J17480–2446 that QPOs at ~ 35 Hz cannot arise due to Lense-Thirring precession if the kHz QPOs are identified as ν_K . For an 11 Hz spin frequency, ν_{LT} should be $\lesssim 0.8$ Hz.

Clearly additional complications are present in the frequency correlations of AMXPs. In this paper we therefore concentrate on the non-pulsating sources. We do include two sources that each have been seen pulsating once for a brief interval, as their aperiodic timing behaviour strongly resembles that of the other sources in our sample (Aquila X-1, Casella et al. 2008 and 4U 1636–53, Strohmayer & Markwardt 2002). Our sample includes the three sources analyzed by van Straaten et al. (2003), but each with a much larger data set, as well as 10 other neutron star LMXBs.

In this paper we present a timing analysis of all RXTE

archival data on 13 neutron star LMXBs. We determine the correlations of the highest frequency kHz QPO (upper kHz QPO) with features at lower frequency using a new, statistically particularly careful method, and report these findings in Section 3. Our results differ from those of van Straaten et al. (2003), as our larger data set allows a better identification of the LF QPOs. In section 4.1.1, we discuss our result in the context of the relativistic precession model and more sophisticated precession models.

2 OBSERVATIONS AND DATA ANALYSIS

We analyze all archival RXTE data on the 13 sources that meet our requirements of known spin, no or only one brief interval of pulsations, and the presence of kHz QPOs. We list these objects along with their respective spin frequencies and observational statistics in Table 2.

2.1 Spectral analysis

We obtain Crab-normalized hard and soft colours for each source from the Standard 2 data following the procedure described in van Straaten et al. (2002). We remove all type I X-ray bursts prior to analysis. The soft colour is defined as the ratio between the counts in the 3.5–6.0 keV and 2.0–3.5 keV energy bands, and the hard colour as the ratio between the 9.7–16.0 keV and 6.0–9.7 keV bands. We use the colours to assess the accretion state of the source (Hasinger & van der Klis 1989).

2.2 Timing analysis

To calculate the power spectra we use Event, Single Bit and Good Xenon data with a time resolution of $1/8192$ s (~ 122 μ s) or better. We take all available energy channels into account (optimizing the energy range depending on QPO type (van Straaten et al. 2000), does not significantly improve the ν_{LT} – ν_K correlation measurement), rebin if necessary to $1/8192$ s, and divide the data into segments of 16 seconds. This results in power spectra with a Nyquist frequency of 4096 Hz and a lowest frequency and frequency resolution of 0.0625 Hz. We do not perform any background or dead time corrections prior to calculating the power spectra but correct for these effects after averaging the Leahy-normalized power spectra. To do so, we subtract a counting noise model spectrum incorporating dead-time effects (Zhang et al. 1995) following the method of Klein Wolt (2004) and renormalize the power spectra such that the square root of the integrated power in the spectrum equals the fractional root mean square (rms) of the variability in the signal (van der Klis 1989).

2.3 Selection of power spectra

We initially average the power spectra obtained within a single observation (RXTE ObsID; typically containing ~ 1.5 ks of data). We then preselect for further analysis those average power spectra that by visual inspection appear to contain QPOs in both the 200–1200 Hz and 0.0625–80 Hz range. For power spectra in which we do not find or significantly fit

the QPOs, we attempt to increase signal to noise by averaging power spectra of multiple observations. We only do this for observations consecutive in time to limit the broadening of narrow components. These consecutive observations differ in colour by $<2\%$, indicating that no state transition occurs between them. The number of observations used for each source are listed in Table 2. The presence of simultaneous high and low frequency QPOs depends on source state, and their detection significance on feature strength and width, as well as the observing time and source brightness. The rejection rate is high for weak sources and sources with many short observations (A 1744–361, EXO 0748–676, XTE J1739–285, 4U 1636–53, 4U 1608–52), as expected. It is also high for sources that mostly populate the high or low hard colour (EXO 0748–676, 4U 1608–52, Aquila X-1, KS 1731–260, SAX J1750.8–2890), as the QPOs are strongest for intermediate hard colour. The sources with the lowest rejection rates are strong (4U 1728–34 and 4U 0614+09) and/or observed at intermediate hard colour for a significant part of the observing campaign (4U 1728–34, 4U 0614+09, 4U 1702–43, 4U 1915–05 and IGR J17191–2821).

2.4 Power spectral fitting

We fit the power spectra with the sum of several Lorentzians. This phenomenological model enables us to monitor the QPOs and band limited noise as the accretion state of the source changes. A Lorentzian can be written as

$$P(\nu) = \frac{(\text{rms})^2 \Delta}{\pi} \frac{1}{(\nu - \nu_0)^2 + (\Delta)^2}, \quad (2)$$

where Δ is the half width at half maximum and ν_0 is the centroid frequency ($P(\nu)$ reaches its maximum here). We fit our model for ν_0 , the power integrated between 0 and infinity, and the quality factor Q , which is a measure of the coherence of the Lorentzian ($Q = \nu_0 / 2\Delta$). In this work we only report ν_0 , because models such as the relativistic precession model predict centroid frequencies. In order to characterize both narrow QPOs and broad power spectral features with ill-constrained centroid frequencies using the same model, characteristic frequencies ($\nu_{\text{max}} \equiv \sqrt{\nu_0^2 + \Delta^2}$) are commonly used (Nowak 2000; Belloni et al. 2002). Lorentzians peak at ν_{max} when plotting $\nu P(\nu)$. For narrow features, ν_{max} and ν_0 will be similar. For broad features however, ν_{max} approaches Δ .

2.5 Naming of power spectral components

We identify power spectral components (see Section 3.1) using the identification scheme and naming convention used by Altamirano et al. (2008) (based on van Straaten et al. 2002) where features are identified (see Figure 1 and Table 1) as break (L_b), second break (L_{b_2}), low frequency QPO (L_{LF}), harmonic of the low frequency QPO (L_{LF_2}), hump (L_h), hectoHz (L_{hHz}), low frequency Lorentzian (L_{low}), lower kHz QPO (L_ℓ), or upper kHz QPO (L_u). This scheme relies on the location of components in the power spectrum, the correlations between characteristic frequencies (ν_{max}) of power spectral components and the similarities in the appearance of power spectra between different sources. We write Q_i and rms_i for the quality factor and fractional rms, respectively,

Component name	Symbol (L_i)
Break	L_b
Second break	L_{b_2}
Low frequency QPO	L_{LF}
Low frequency QPO harmonic	L_{LF_2}
Hump	L_h
HectoHz	L_{hHz}
Low frequency Lorentzian	L_{low}
Lower kHz QPO	L_ℓ
Upper kHz QPO	L_u

Table 1. Identification scheme of power spectral components used in this paper, see Figure 1.

Source	Spin (Hz)	Obs. in Archive	Obs. used
4U 1728–34	363	423	210
4U 0614+09	415	494	164
4U 1636–53	581	1555	83
4U 1702–43	329	255	72
4U 1608–52	620	1072	43
Aquila X-1	550	583	40
KS 1731–260	524	86	22
4U 1915–05	270	56	21
IGR J17191–2821	294	19	11
SAX J1750.8–2900	601	129	7
XTE J1739–285	1122	9	-
A 1744–361	530	53	-
EXO 0748–676	552	749	-

Table 2. The sources included in our sample. The neutron star spin frequency was inferred from burst oscillations (or from intermittent pulsations in 4U 1636–53 and Aquila X-1). (Watts 2012; Ritter & Kolb 2003).

of component L_i . We discuss the identification of features for all sources together in Section 3.1. A detailed discussion of each source in our sample can be found in Appendix 2.

2.6 Power law fitting

In order to compare our measured QPO frequencies to model predictions, we fit power laws (of the form $y = a \cdot x^b$) to the sample of (ν_{LT} , ν_K) measurements.

Our measurements have asymmetric errors in both coordinates. Rather than relying on an approximate method such as converting to logspace and symmetrizing the error bars to be able to use a 2-dimensional linear regression method, we introduce a new fitting method that is mathematically identical to performing a fit to all power spectra simultaneously with the frequency pair (ν_{LT} , ν_K) tied via a power law relation. This method is described in Appendix A.

3 RESULTS

We present our best-fit power laws in Table 3. We find that A 1744–361, EXO 0748–676 and XTE J1739–285 are unsuitable for further analysis due to low signal to noise. With our data selection and averaging criteria (see Section 2.3) we fail to detect the upper kHz QPO in these sources above a significance level of 2σ .

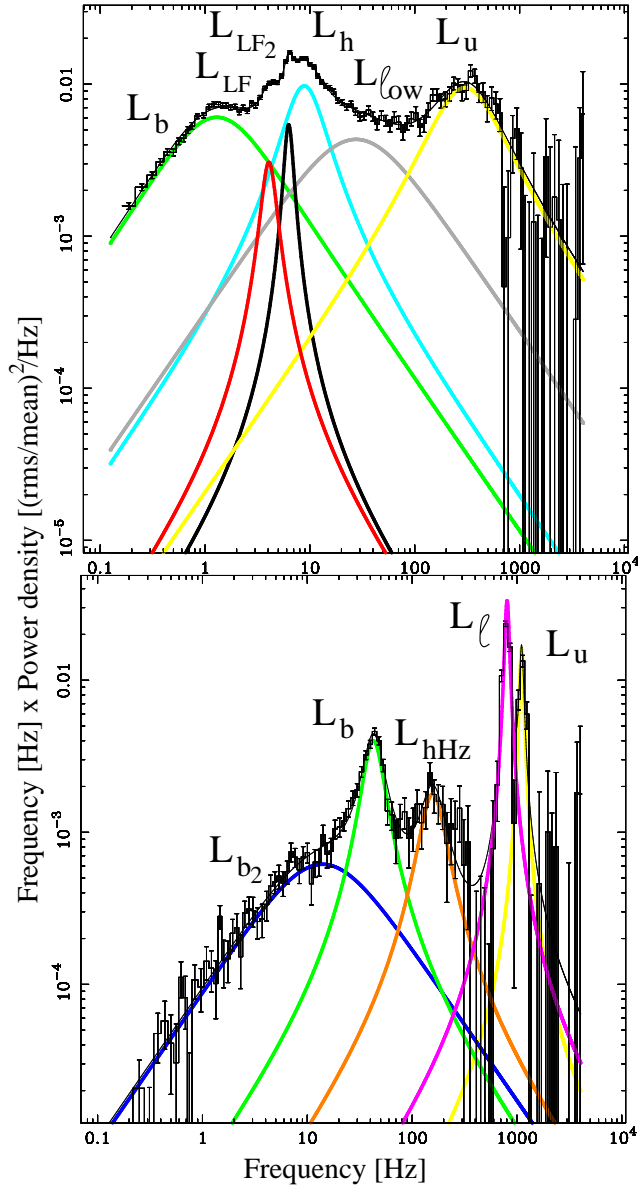


Figure 1. Representative power spectra of two different accretion states of 4U 1728–34 illustrating the naming scheme we use. The top and bottom panel are the same as panel A and D, respectively, in Figure 4.

3.1 Identification of power spectral features

In Figure 2 we plot all measured frequencies for all sources vs. the upper kHz QPO frequency. Since we use centroid frequency (ν_0), the correlations traced out differ from those based on ν_{\max} . As a result, the ν_{\max} -based classification of (especially the broad) features does not necessarily agree with one that would have likely been used based on the centroid frequency correlations. To illustrate this we plot the same results converted to ν_{\max} in Figure 3. Notable differences include the L_b vs. L_{b_2} and L_h vs. L_{hHz} identifications. Also note the more pronounced flattening of the centroid frequency relations below $\nu_u \sim 350$ Hz as compared to ν_{\max} . We comment below on how these issues could affect the ν_{LT} - ν_K relations that are the subject of this paper.

In order to fit power laws to the frequency correlations we divide the data into groups, as indicated by the ellipses in Figure 2. The precise frequency ranges defining these groups for each source can be found in Table C3. Group 1 is composed of power spectra with a broad upper kHz QPO (see Section 3.1.2), Group 3 comprises power spectra in which we do not simultaneously fit L_h and L_{hHz} , or with $\nu_u > 1000$ (see Sections 3.1.3 and 3.1.4 for more detail). In Figures 4 and 5 we show the representative power spectra for 4U 1728–34, 4U 0614+09, 4U 1608–52, 4U 1636–53, 4U 1702–43 and Aquila X-1. The upper kHz QPO frequency (ν_u) increases from ~ 250 Hz in row A, via ~ 500 Hz in row B and ~ 700 Hz in row C, to ~ 1000 Hz in row D. Clearly, the power spectra in each row are very similar. The colours of the best-fit Lorentzian components plotted correspond to those used for plotting their respective frequencies in Figures 2 and 3. The centroid frequency of broad Lorentzians (L_b , L_{b_2} , L_{low} and L_{hHz}) can be very small and even slightly negative; they are therefore not always present in our logarithmic centroid frequency-frequency plots. When a negative centroid frequency occurs in a fit, we fix it to 0.

3.1.1 The break and second break Lorentzians

We identify L_b and L_{b_2} by their appearance in the power spectrum. At $\nu_u < 700$ Hz (rows A–C in Figure 4), L_b (green) is the broad component with the lowest frequency. For $\nu_u > 700$ Hz (row D in Figure 4), Q_b increases and a separate broad low frequency component is needed to obtain a satisfactory power spectral fit, this is L_{b_2} (dark blue). So, the identification of L_b and L_{b_2} is straightforward and confirmed by the $\nu_{u,\max}$ vs. $\nu_{b,\max}$, $\nu_{u,\max}$ vs. $\nu_{b_2,\max}$ frequency correlations, see Figure 3. In order to keep the link to earlier works, we maintain the ν_{\max} -based identifications for these low frequency features, in spite of the different behaviour of ν_b above and below $\nu_u \sim 700$ Hz when plotting centroid frequencies (see Figure 2). Since Q_b increases for $\nu_u > 700$ Hz, we regard L_b as a candidate for precession and fit power laws to the ν_b - ν_u frequency pairs when $Q_b > 0.5$. The second break Lorentzian, L_{b_2} , is a broad feature that is often best characterized by a zero-centered Lorentzian.

3.1.2 The LF, LF₂ QPOs and hump Lorentzians

In rows B and C ($\nu_u \sim 500$ Hz), Group 2 in Figure 2, the identification of L_{LF} (red) and L_h (cyan) again is straightforward. Our power spectra closely resemble those previously reported in the literature (see Figure 1) and ν_h and ν_{LF} fall on different correlations (with always $\nu_h > \nu_{LF}$) both in ν_{\max} and ν_0 (van Straaten et al. 2002; Altamirano et al. 2008). We find that for $\nu_u > 400$ Hz, Q_h increases, Q_{LF} stays roughly constant, rms_h decreases, and rms_{LF} reaches a maximum at $\nu_u \sim 600$ Hz and then decreases as ν_u increases (see Figures 6 and 7).

The correlations traced out by ν_h and ν_{LF} flatten in some sources when $\nu_u < 400$ Hz (For instance in 4U 1728–34, Group 1, see Figure C1). This effect is less pronounced in the ν_{\max} representation. It can be explained by L_u becoming broader at low (< 400 Hz) frequency (compare L_u (yellow) in row A to L_u in row B in Figures 4 and 5).

When we fit two narrow QPOs and a broad component at

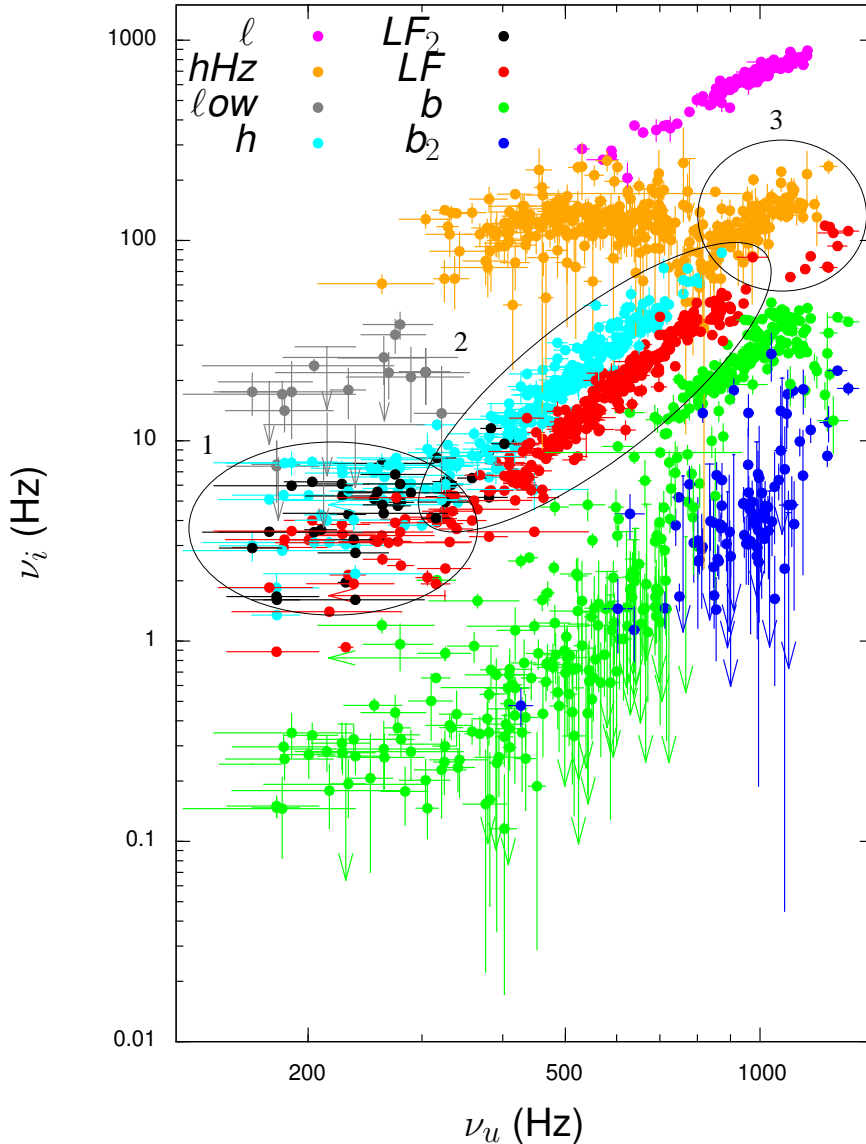


Figure 2. Frequencies of all sources plotted against the upper kHz QPO frequency. We fit power laws to distinct groups that appear to be present in both the LF QPO and hump feature. For clarity, we indicate the 98% upper limit to frequencies of broad *low*, hHz, b and b_2 Lorentzians with arrows.

low frequency we identify them, in order of increasing centroid frequency, as L_{LF} (red), L_{LF_2} (black), and L_h (cyan). As can be seen in Figures 4 and 5 (for instance, in row A, compare 4U 1728–34 and Aquila X-1), L_{LF} and L_{LF_2} are not always simultaneously present. In Figure 7 we see that the Q-values of L_{LF} and L_{LF_2} are similar for $\nu_u < 400$ Hz. Identification based solely on the appearance of these features in the power spectrum is therefore not straightforward. To resolve the ambiguity in this identification, we use the respective correlations of ν_{LF_2} and ν_{LF} with ν_h as an additional tool to correctly differentiate between these low frequency QPOs (see Figure 8). We note that centroid frequencies of L_b , L_{LF} , L_{LF_2} , and L_h roughly follow $\nu_{LF}/\nu_h = 0.4-0.7$, $\nu_{LF_2} \approx \nu_h$ and $\nu_b/\nu_h = 0.15-0.3$. As can be seen from Figures 8 and 9, there is no strong evidence for harmonic relations between any two components. Furthermore, for L_{LF} and L_h , rms and Q

behave differently when plotted vs. ν_u (see Figures 6 and 7) suggesting a different physical origin for these features. We discuss the identification of L_{LF} in Group 3 in section 3.1.4.

3.1.3 HectoHz, low frequency Lorentzians and kHz QPOs

We identify the broad component with $\nu \sim 100$ Hz in rows B-C of Figures 4 and 5 as L_{hHz} (orange). We find that for $\nu_u > 700$ Hz, i.e. in Group 3, Q_{hHz} increases while ν_{hHz} falls on the extrapolation of the correlation traced out by ν_h - ν_u . In the ν_{\max} representation this is not obvious. We do not detect a separate L_h (with an expected frequency around ~ 100 Hz) in power spectra with $\nu_u > 700$ Hz; we therefore suspect that we are fitting a blend of L_h and L_{hHz} there. The low frequency Lorentzian (L_{low} , gray) is a broad feature with $\nu_{hHz} > \nu_{low} > \nu_h$ and $Q_{low} > Q_h$ which is occasionally needed to

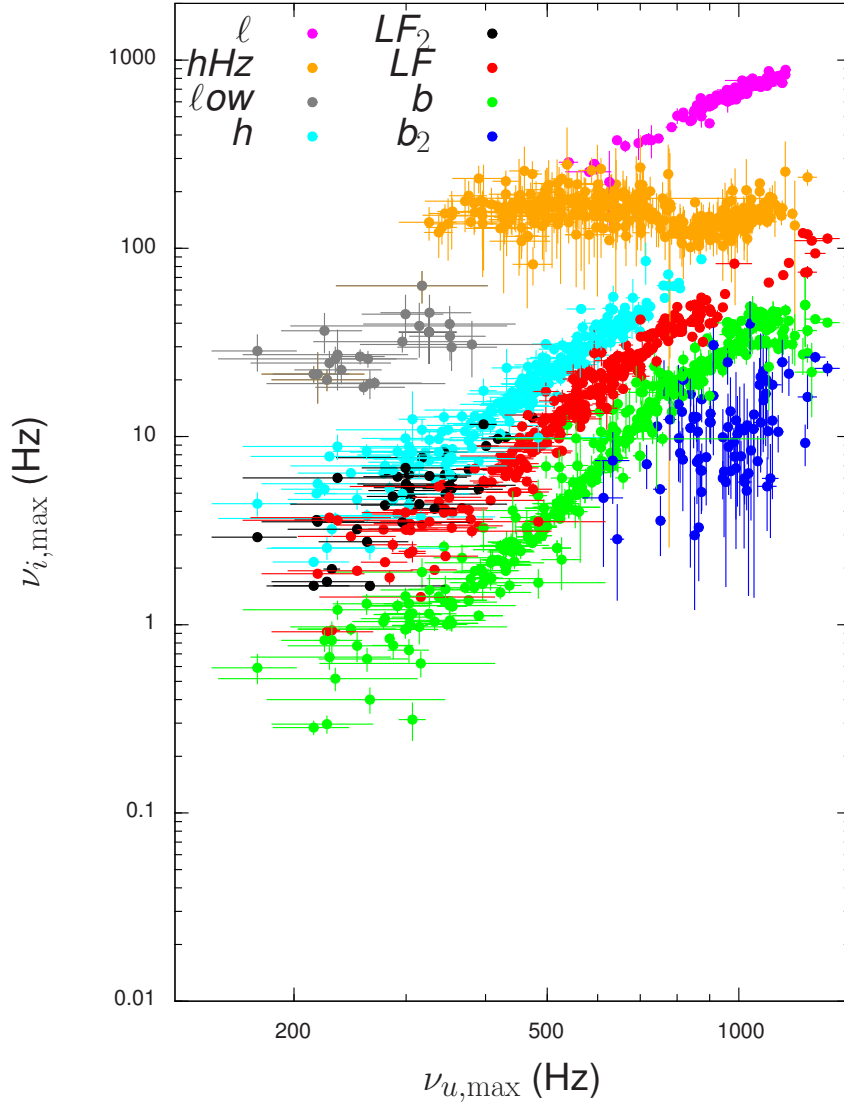


Figure 3. As in Figure 2, but with ν_{\max} .

fit the broad band noise between L_h and L_u in power spectra such as illustrated in row A of Figures 4 and 5. Finally, of the kHz QPOs, L_u (yellow) is always the component with the highest frequency in the power spectrum. The lower kHz QPO L_ℓ (magenta) appears in rows C and D in Figures 4 and 5. Always, $\nu_u > \nu_\ell > \nu_{hHz}$ and also $Q_\ell > Q_{hHz}$.

3.1.4 Power spectra with high ν_u

We find characteristic power spectra with ν_u in the 1000–1400 Hz range (in Group 3 of Figure 2) for 4U 1728–34 (3 cases), 4U 0614+09 (5 cases), 4U 1702–43 (1 case) and Aquila X-1 (1 case; see Figure 10 for examples), at relatively high luminosity and low hard color. They are similar to the power spectra illustrated in row D of Figures 4 and 5, but need to be fitted with an extra Lorentzian below 100 Hz. As data are sparse for these high values of ν_u we have to extrapolate the frequency and rms trends for the feature identification. The centroid frequency of the extra Lorentzian falls between

ν_{hHz} (orange) and ν_b (green), and roughly on the extrapolation of the $\nu_{LF}-\nu_u$ correlation when plotted vs. ν_u . We tentatively identify this component as ν_{LF} (red). In 4U 1728–34 we identify the Lorentzian with a centroid frequency of 234.5 Hz as L_{hHz} (orange, top panel of Figure 10). Its frequency falls on the extrapolation of the $\nu_h-\nu_u$ correlation (Figure 2), however when regarding the Lorentzian as L_h , ν_{LF} does not behave as expected from Figure 8. We consider the identifications of L_{LF} and L_{hHz} in this case as ambiguous.

We use the extrapolation of the $\nu_b-\nu_u$ and $\nu_{b2}-\nu_u$ correlations at lower frequencies for the identification of L_b (green) and L_{b2} (dark blue) in the power spectra with $\nu_u > 1000$ Hz, see Figure 2.

3.1.5 Best-fit power laws

In Table 3 we present the parameters of the best-fit power laws to our frequency groups specified in Table C3. In the last column we quote the upper and lower limits on power

law indices and associated confidence levels to illustrate the deviation of the best-fit power law index from the RPM-prediction of 2.0. When we assess this significance, we cap the fraction of extrapolated χ^2 maps used for our power law fits (see Appendix A) to $<10\%$, which leads to different values for the limits quoted. Overall, the best-fit power law index exceeds 2.0 in 80% of the cases at $>3\sigma$. In 4U 1728–34 and 4U 0614+09 the best-fit power law index to ν_{LF} and ν_h in Group 2 is in excess of 2.2 at $>10\sigma$.

The best-fit power laws to frequencies in Group 2 significantly differ from one another, see Figures 11, 12, 13 where we show the confidence contours for the best-fit power law index and normalization.

Interestingly, power laws fitted to ν_{LF} in Groups 2 and 3 combined in 4U 1728–34, 4U 0614+09, 4U 1702–43 and Aquila X-1 all have indices that are somewhat lower than the power laws fitted to ν_{LF} in Group 2 alone (for ν_h this is not the case). This might indicate a change in power law index as ν_u increases. However, the differences in index are not very significant. To further test this possibility, and also because the identification of ν_{LF} in Group 3 is somewhat ambiguous (as explained in Section 3.1.4), we fit power laws to frequencies below (Group 2a) and above (Group 2b) $\nu_u=600$ Hz in Group 2 in 4U 1728–34 and 4U 0614+09. We use these two sources as they have the largest data sets. In 4U 1728–34, we indeed find that the power law index is lower for ν_{LF} in Group 2b than 2a, see Table 3 (at 2.28 ± 0.03 it is still in excess of 2.1 at 7σ). For 4U 0614+09 no significant flattening towards higher frequency is detected by this method.

Although we obtain a reduced χ^2 of ~ 1 , the corresponding formal probabilities are typically low. This is the result of a combination of small deviations of the power spectral model from the data and fitting many power spectra simultaneously. The fits to individual power spectra are all acceptable, see Table C2 for the χ^2/dof .

3.2 Comparison to earlier work

The power law indices we find are similar to earlier results from van Straaten et al. (2000) on 4U 0614+09 in which a power law index of 2.46 ± 0.07 was reported for the ν_{LF} - ν_u correlation. In that work the averaging of power spectra was limited due to a small data set. In later work on 4U 1728–34 (Ford & van der Klis 1998; van Straaten et al. 2002), 4U 0614+09 (van Straaten et al. 2002) and 4U 1608–52 (van Straaten et al. 2003), the authors found power laws with indices of around 2.0. In these studies many power spectra with similar colours were averaged which led to considerable broadening of, in particular, L_{LF} . The resulting blend of L_{LF} and L_h was then fitted with a single Lorentzian.

With our strict data selection and averaging rules and careful identification we are able to detect and separately fit both L_{LF} and L_h over a large range of ν_u . In Figure 14 we illustrate this using an observation of 4U 1728–34 used in van Straaten et al. (2002) and in our analysis, fitted with 5 (upper panel, as in the literature) and 6 (lower panel, as in our work) components. We find the fit is significantly bet-

ter when fitting L_{LF} and L_h as two components (F-statistic probability $P=0.53 \times 10^{-14}$).

We find that as ν_u increases, L_{LF} becomes stronger compared to L_h (rms_h/rms_{LF} drops, Q_h/Q_{LF} rises but is always <1 , see Figures 6 and 7) and L_h blends with L_{hHz} . Due to these effects, a blend of L_{LF} and L_h is fit with a centroid frequency close to ν_h for low ν_u , and close to ν_{LF} for high ν_u . This results in a shallower power law when fitting the frequency correlation with ν_u . We plot the frequencies and best-fit power law with index 2.01 reported in van Straaten et al. (2002) (black) together with our results (blue and red) for 4U 1728–34, 4U 0614+09 and 4U 1608–52 in Figure 15. Our best-fit power laws are characterized by indices significantly higher than 2, as reported in Table 3.

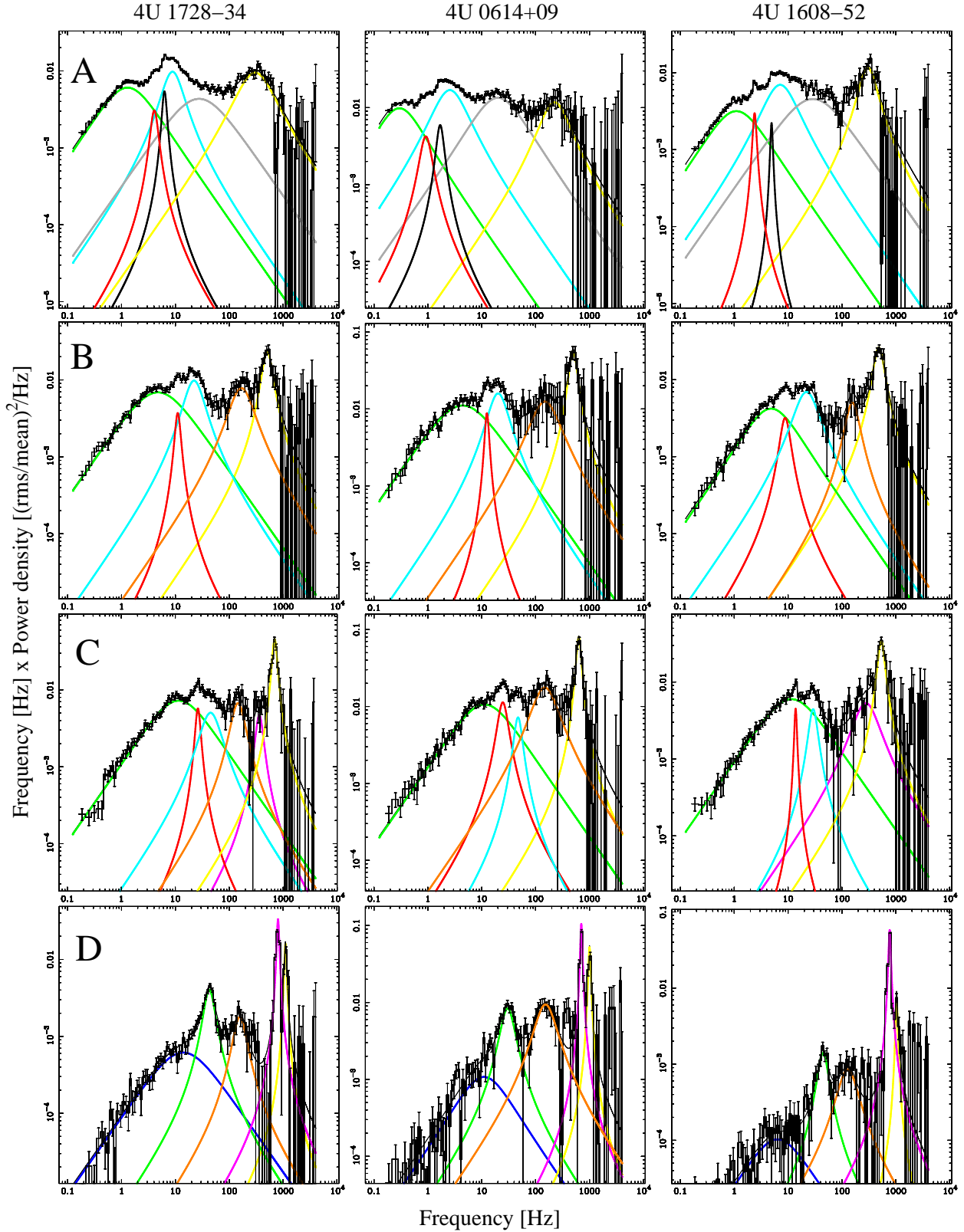


Figure 4. Representative power spectra of 4U 1728-34, 4U 0614+09 and 4U 1608-52 in different accretion states. Colours correspond with Figure 2. The frequency of the upper kHz QPO (yellow) increases from ~ 250 Hz in row A, via ~ 500 Hz in row B and ~ 700 Hz in row C, to ~ 1000 Hz in row D. The low frequency QPO (L_{LF} , red) and the hump component (L_h , cyan) are present in rows A-C. The low frequency QPO is accompanied by its 'harmonic' (L_{LF2} , black) in row A. The lower kHz QPO (L_ℓ , magenta) shows up in row D, as well as an extra low frequency noise component (L_{b2} , dark blue). The break and hHz noise components L_b (green) and L_{hHz} (orange) are present in all power spectra shown here, L_{low} (gray) is only present in row A. The observations used in this figure are listed in Table C1.

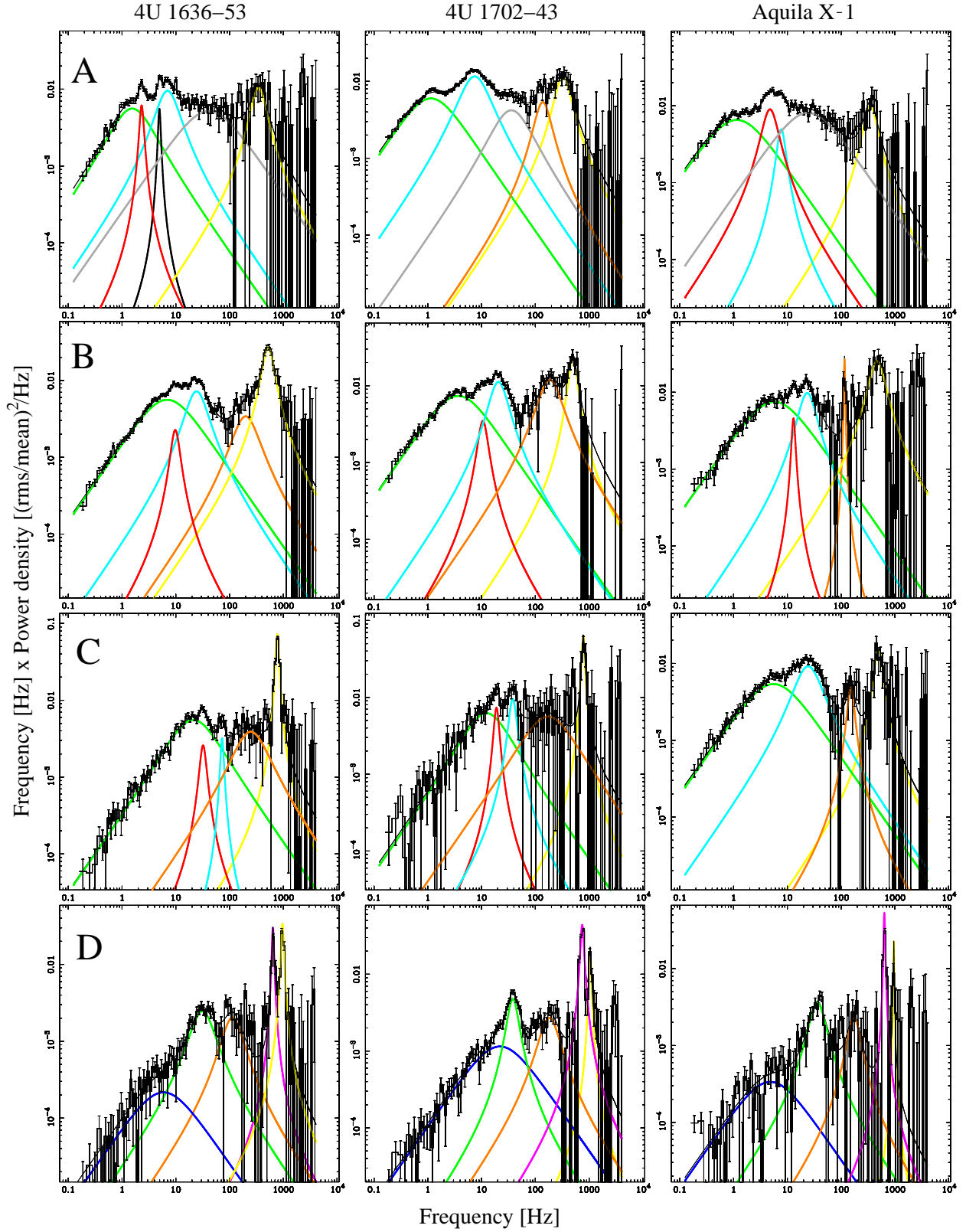


Figure 5. As in Figure 4, but for 4U 1636-53, 4U 1702-43 and Aquila X-1.

Source	L_i	Group	No. of freq. pairs (v_i, v_u)	Norm. (Hz) at $v_u=600$ Hz	Index	Reduced χ^2 (dof)	Limit on index (significance)
4U 1728–34	LF	1	12	5.1 ± 0.2	$0.43^{+0.04}_{-0.06}$	1.10 (3864)	<0.8 (3.3σ)
	h	1	11	11.2 ± 1.1	0.66 ± 0.13	1.08 (3541)	<2.0 (5.0σ)
	LF	2	133	$17.79^{+0.04}_{-0.07}$	2.47 ± 0.01	1.05 (43389)	>2.2 (23.9σ)
	h	2	103	29.4 ± 0.2	$2.64^{+0.04}_{-0.03}$	1.05 (33626)	>2.2 (13.4σ)
	LF	2+3	136	17.8 ± 0.1	2.45 ± 0.01	1.05 (44509)	>2.2 (21.2σ)
	LF	2a	56	$5.9^{+0.1*}_{-0.2}$	$2.76^{+0.11}_{-0.08}$	1.08 (18258)	>2.5 (10.0σ)
	LF	2b	77	$36.0 \pm 0.1^{**}$	2.28 ± 0.03	1.03 (25133)	>2.1 (7.0σ)
	h	2+3	161	29.5 ± 0.2	2.75 ± 0.02	1.06 (53366)	>2.4 (17.0σ)
4U 0614+09	b	-	62	6.1 ± 0.1	$3.09^{+0.03}_{-0.04}$	1.07 (21573)	>2.6 (12.6σ)
	LF	2	70	$20.9^{+0.2}_{-0.1}$	$2.63^{+0.03}_{-0.04}$	1.04 (22708)	>2.2 (13.4σ)
	h	2	55	$36.4^{+0.6}_{-0.5}$	2.95 ± 0.05	1.06 (17785)	>2.4 (11.4σ)
	LF	2+3	75	21.0 ± 0.1	$2.58^{+0.03}_{-0.02}$	1.05 (24772)	>2.2 (14.1σ)
	LF	2a	32	$7.1^{+0.2*}_{-0.1}$	2.69 ± 0.07	1.06 (10497)	>2.3 (5.5σ)
	LF	2b	38	$44.4 \pm 0.4^{**}$	2.57 ± 0.06	1.02 (12213)	>2.2 (6.3σ)
	h	2+3	98	$34.8^{+0.3}_{-0.4}$	$2.70^{+0.03}_{-0.02}$	1.05 (32346)	>2.5 (9.5σ)
	b	-	58	11.7 ± 0.1	1.48 ± 0.02	1.04 (19926)	<2.0 (14.1σ)
4U 1608–52	LF	2	14	19.0 ± 0.9	$2.78^{+0.09}_{-0.11}$	1.06 (4388)	>2.5 (6.3σ)
	h	2	14	$38.4^{+1.9}_{-1.8}$	2.51 ± 0.10	1.05 (4388)	>2.1 (3.5σ)
	h	2+3	23	41.2 ± 0.8	2.56 ± 0.03	1.40 (8136)	>2.2 (7.7σ)
	b	-	15	$8.5^{+0.3}_{-0.4}$	$3.05^{+0.09}_{-0.07}$	1.58 (5722)	>2.6 (5.7σ)
4U 1702–43	LF	2	15	19.4 ± 0.4	2.51 ± 0.07	1.07 (4882)	>2.2 (3.9σ)
	h	2	12	$34.4^{+2.5}_{-1.9}$	$2.56^{+0.23}_{-0.20}$	1.06 (3902)	>2.1 (3.6σ)
	LF	2+3	16	$19.0^{+0.3}_{-0.4}$	2.25 ± 0.05	1.08 (5210)	>2.0 (3.2σ)
	h	2+3	20	34.8 ± 0.9	2.59 ± 0.07	1.08 (6561)	>2.2 (5.4σ)
	b	-	10	$7.9^{+0.8}_{-0.6}$	$2.64^{+0.13}_{-0.18}$	1.09 (3314)	>2.0 (4.5σ)
4U 1636–53	LF	2	24	$14.9^{+0.1}_{-0.2}$	$2.69^{+0.03}_{-0.02}$	1.01 (7734)	>2.6 (4.5σ)
	h	2	22	$33.1^{+0.7}_{-0.8}$	$2.85^{+0.12}_{-0.09}$	1.01 (7154)	>2.5 (3.7σ)
	h	2+3	35	$33.4^{+0.5}_{-0.6}$	$2.91^{+0.04}_{-0.03}$	1.06 (11381)	>2.5 (10σ)
	b	-	17	7.3 ± 0.3	$3.05^{+0.01}_{-0.08}$	1.15 (5464)	>2.8 (3.2σ)
4U 1915–05	LF	2	15	$13.9^{+0.4}_{-0.6}$	$2.53^{+0.13}_{-0.11}$	1.05 (4947)	>2.1 (4.5σ)
Aquila X-1	LF	2	15	23.3 ± 0.7	$2.42^{+0.08}_{-0.10}$	1.04 (5067)	>2.1 (3.6σ)
	h	2	28	$36.3^{+0.6}_{-1.0}$	2.35 ± 0.04	1.05 (9316)	>2.2 (3σ)
	LF	2+3	16	$21.5^{+0.3}_{-0.2}$	$2.13^{+0.02}_{-0.03}$	1.04 (5393)	>2.0 (4.8σ)
	h	2+3	29	$36.3^{+0.6}_{-0.8}$	$2.35^{+0.04}_{-0.03}$	1.06 (9701)	>2.2 (3.8σ)
	b	-	3	$10.9^{+1.5}_{-1.4}$	$2.38^{+0.28}_{-0.34}$	1.04 (1036)	>2.0 (1.0σ)
KS 1731–260	LF	2	10	15.2 ± 0.8	$2.22^{+0.11}_{-0.10}$	1.07 (3237)	>2.0 (3.2σ)
	h	2	11	$26.9^{+1.4}_{-1.2}$	$1.93^{+0.12}_{-0.10}$	1.07 (3493)	<2.0 (0.6σ)
SAX J1750.8–2900	LF	2	3	$15.2^{+1.1}_{-9.6}$	$2.95^{+0.21}_{-0.22}$	0.98 (981)	>2.4 (2.2σ)
	h	2	4	$25.0^{+3.2}_{-3.8}$	$3.32^{+0.70}_{-0.52}$	0.97 (1312)	>2.0 (3.0σ)
	b	-	2	$5.7^{+10.5}_{-4.6}$	$3.24^{+3.46}_{-1.97}$	0.89 (662)	>2.0 (0.7σ)
IGR J17191–2821	b	-	4	$10.6^{+1.4}_{-1.8}$	$2.45^{+0.32}_{-0.21}$	0.97 (1439)	>2.0 (1.7σ)

Table 3. Power law fit parameters for v_i vs. v_u correlations. See the main text for explanation of groups. When we fit v_h in Group 2+3, we include the v_{hHz} measured in Group 3 as v_h . We use v_b for the power law fits to the v_b - v_u correlation only when $Q_b > 0.5$. Errors quoted here use $\Delta\chi^2=1$. (* normalization at $v_u = 400$ Hz, ** normalization at $v_u = 800$ Hz.)

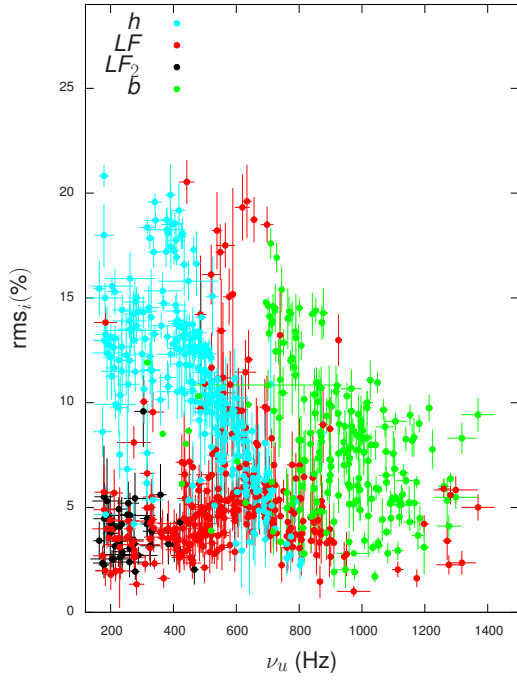


Figure 6. Fractional rms levels of L_u , L_h , L_{LF} , L_{LF_2} , and L_b (L_b for $Q_b > 0.5$ only) vs. upper kHz QPO frequency in all sources.

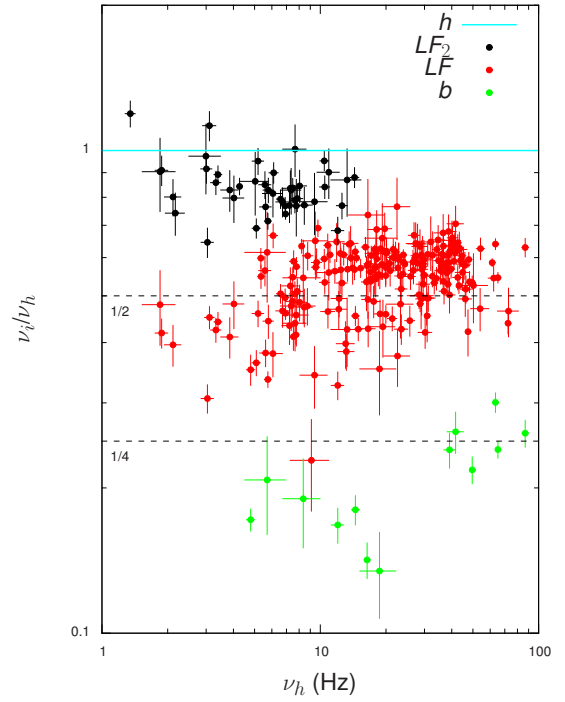


Figure 8. Best-fit ν_{LF_2} , ν_{LF} and ν_b of all sources divided by ν_h , plotted vs. ν_h .

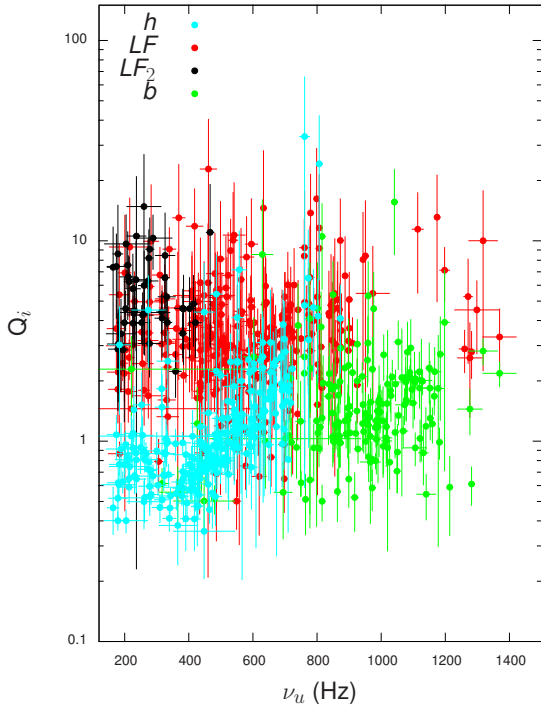


Figure 7. Q-factors of L_u , L_h , L_{LF} , L_{LF_2} , and L_b (L_b for $Q_b > 0.5$ only) vs. upper kHz QPO frequency in all sources.

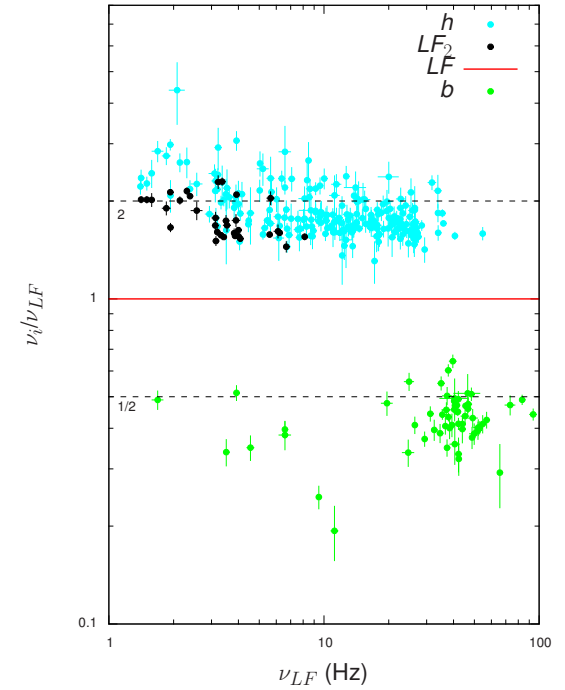


Figure 9. Best-fit ν_{LF_2} , ν_h and ν_b of all sources divided by ν_{LF} , plotted vs. ν_{LF} .

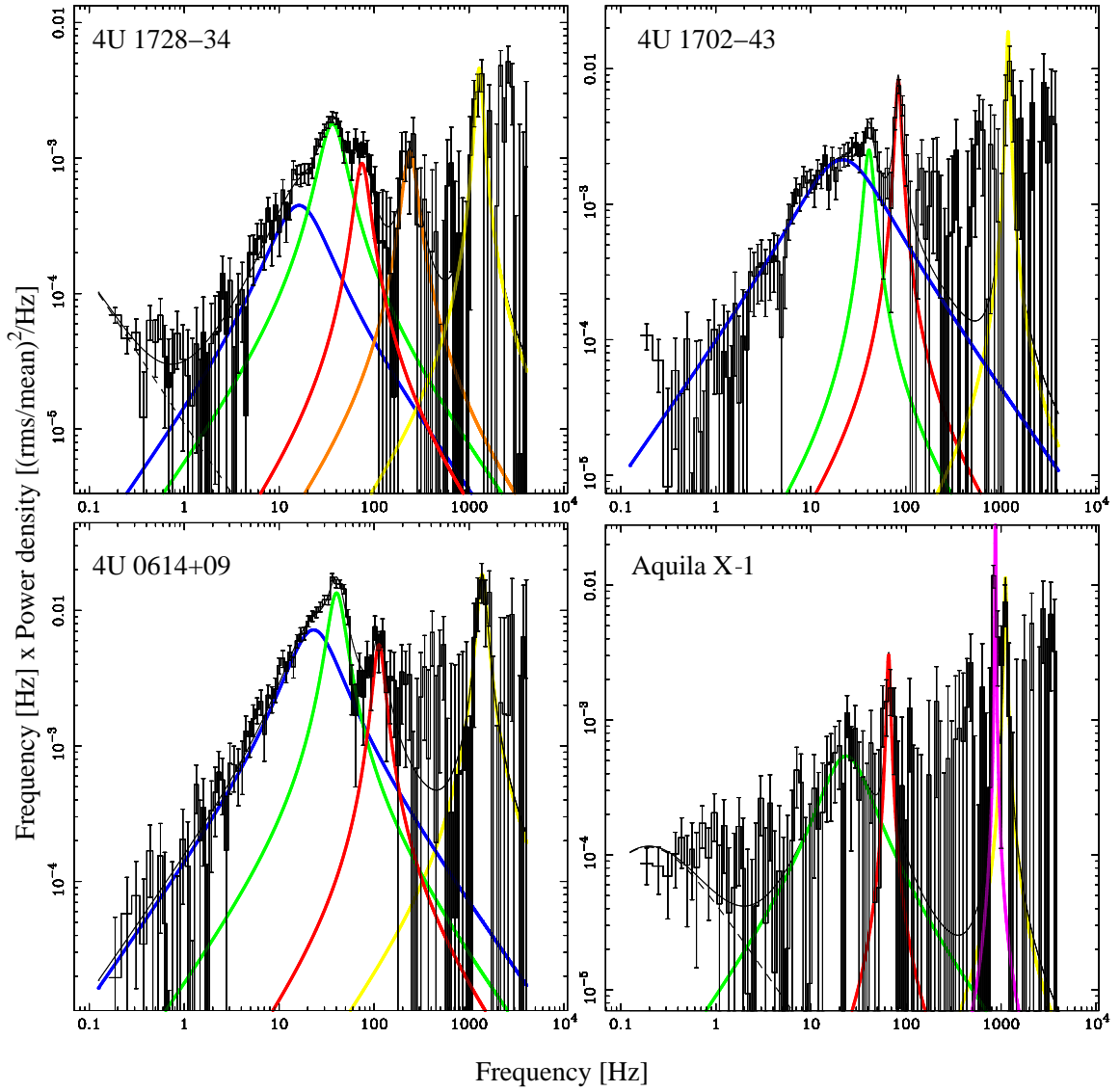


Figure 10. Examples of power spectra of 4U 1728–34, 4U 0614+09, 4U 1702–43 and Aquila X-1 with the highest ν_u , all found at high luminosity. The frequencies fall in Group 3, shown in Figure 2. The power spectra have similar upper kHz QPOs (*yellow*) with $\nu_u > 1000$ Hz, and are accompanied by QPOs with $70 < \nu < 100$ Hz. We tentatively identify the latter as ν_{LF} (*red*), see text. The observations used in this figure are listed in Table C1, in the column “High ν_u ”.

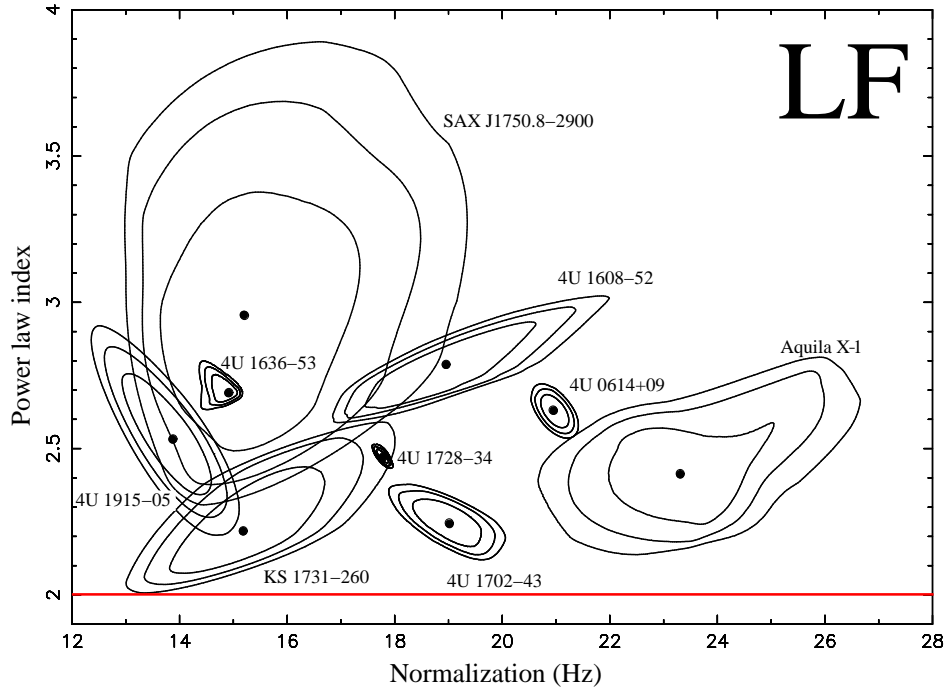


Figure 11. Confidence contours for the best-fit power law index and normalization at $\nu_u=600$ Hz of the $\nu_{LF}-\nu_u$ correlations in each source, with ν_{LF} in Group 2 (see Table 3). We plot the 75% (inner), 95% (middle) and 99% (outer) two-parameter confidence limits (corresponding to $\Delta\chi^2=3.13, 6.17$ and 9.21 , respectively). The best-fit values are indicated by the dots, the red line corresponds a power law index of 2.

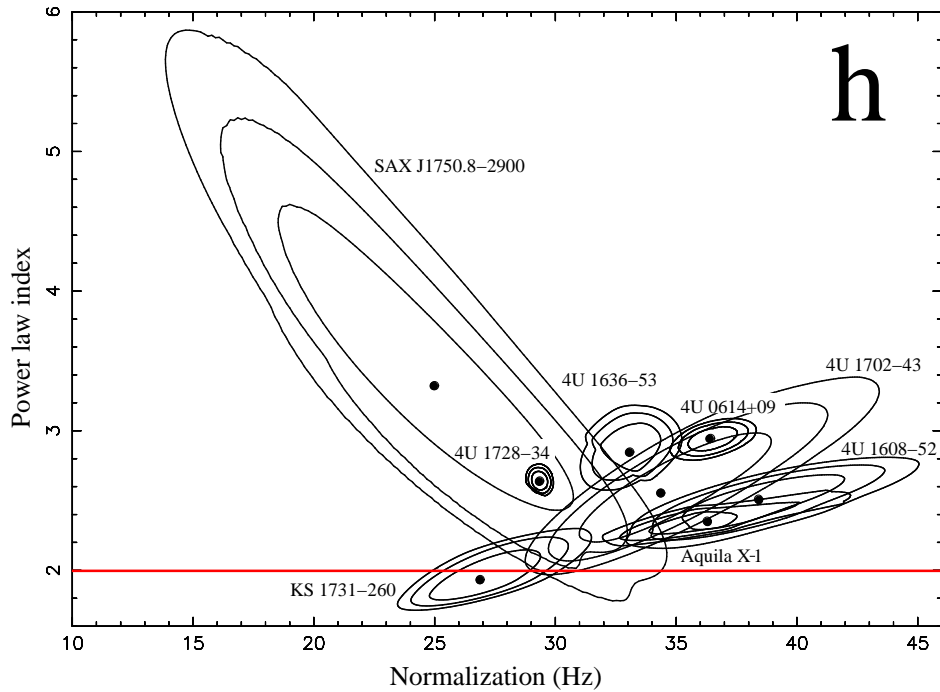


Figure 12. As in Figure 11, but for the $\nu_h-\nu_u$ correlations (with ν_h in Group 2).

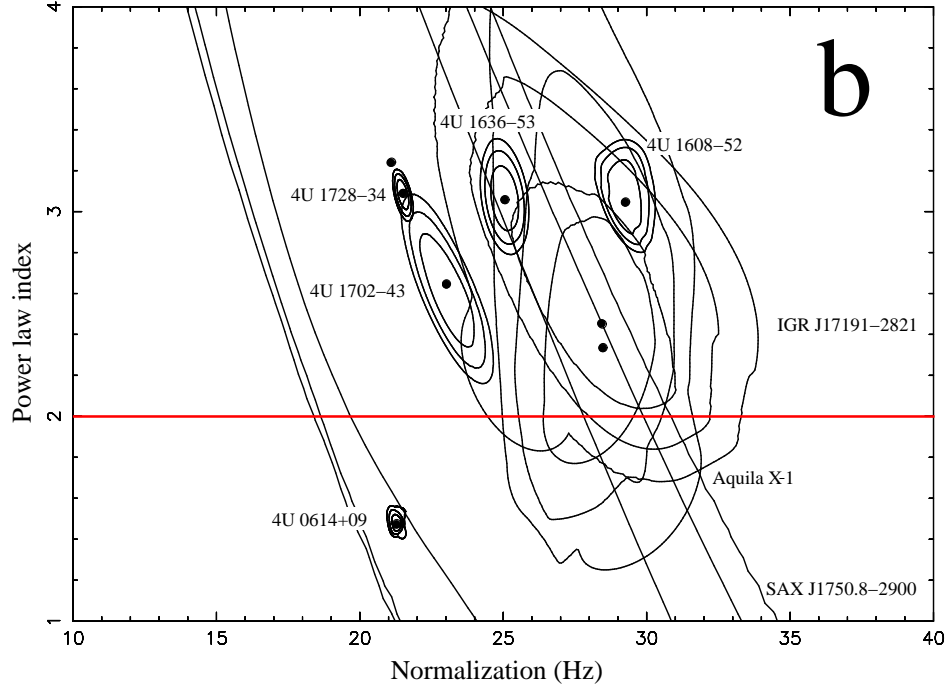


Figure 13. As in Figure 11, but with the normalization at 900 Hz, for the ν_b - ν_u correlations including ν_b only when $Q_b > 0.5$.

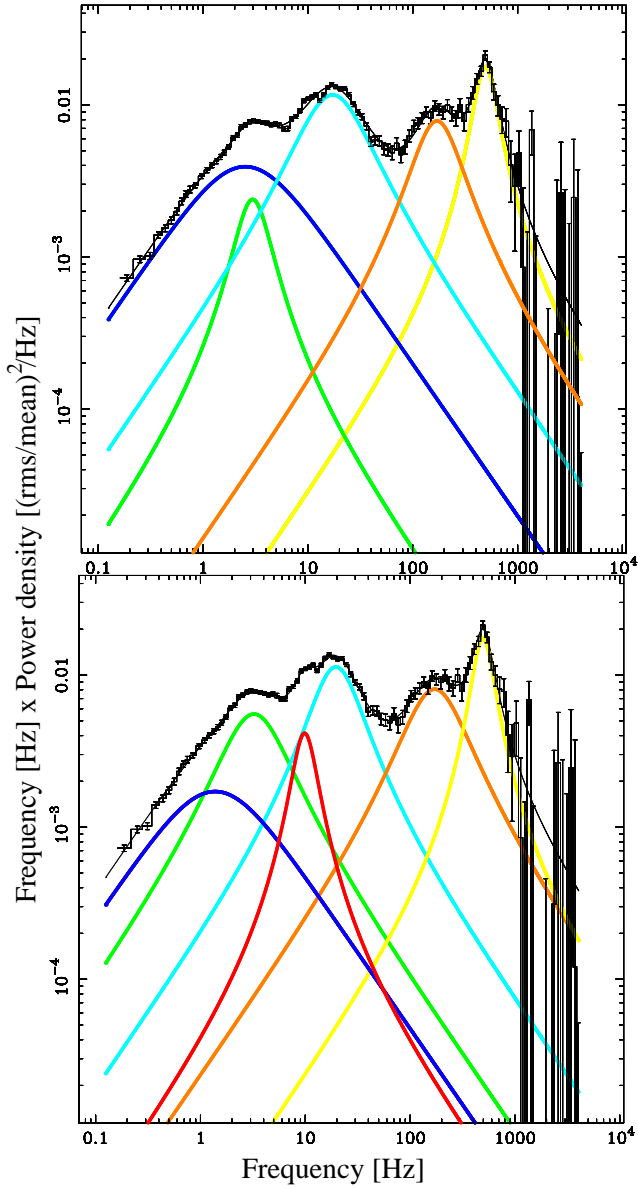


Figure 14. Upper panel: fit to the power spectrum of an observation of 4U 1728–34 (10073-01-07-000) with 5 Lorentzians as in [Di Salvo et al. \(2001\)](#); [van Straaten et al. \(2002\)](#) ($\chi^2/\text{dof}=425/327$). Lower panel: fit with 6 Lorentzians ($\chi^2/\text{dof}=343/324$).

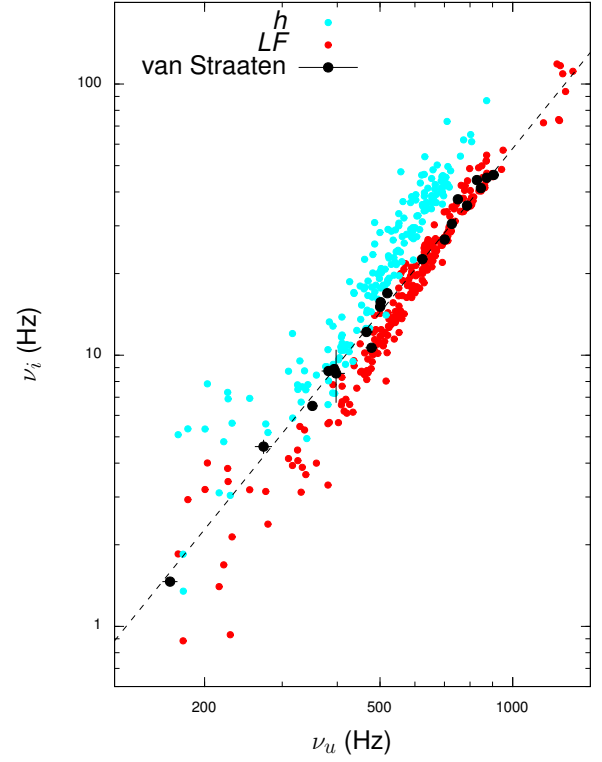


Figure 15. Frequencies previously reported by [van Straaten et al. \(2003\)](#) in the range predicted for the Lense-Thirring precession frequency for 4U 1728–34, 4U 0614+09 and 4U 1608–52 plotted together with our results for these sources. The dashed line is the best-fit power law with index 2.01 reported in [van Straaten et al. \(2003\)](#).

4 DISCUSSION

We inspected power spectra of a sample of 13 NS-LMXBs and in a careful analysis measured the centroid frequency correlations of three different peaks with $\nu < 80$ Hz; L_h , L_{LF} and L_b with always $\nu_h > \nu_{LF} > \nu_b$. We found that more indiscriminate averaging of power spectra than performed by us led previous authors (e.g., [van Straaten et al. 2003](#)) to fit L_h and L_{LF} as a single blended feature which has a correlation with ν_u that is less steep than those obtained for the individual components. Our results are in correspondence with previous studies using small data sets or those in which power spectra were averaged over a limited time span ([van Straaten et al. 2000](#); [Altamirano et al. 2008](#)). We note that while the frequencies of L_h , L_{LF} and L_b depend similarly on ν_u , their rms dependencies on ν_u markedly differ (see Figure 6), suggesting differences in their formation physics.

For the correlations of ν_{LF} , ν_h and ν_b vs. ν_u we find best-fit power law indices that are significantly higher than 2 for all well constrained sources in our sample; see Table 3. We find that the frequencies of power spectral components behave similarly in 4U 1728–34, 4U 0614+09, 4U 1608–52, 4U 1702–43 and 4U 1636–53 when plotted against ν_u . The correlations of ν_{LF} , ν_h and ν_b with ν_u we fit in these sources are very similar, but not identical, as the joint probability distributions of the power law indices and normalizations differ significantly (see Figures 11, 12 and 13).

Aquila X-1, KS 1731–260, SAX J1750–2900, IGR J17191–2821, and 4U 1915–05 have either low signal to noise or a small data set. The QPOs we find in these sources appear similar to the first group but their identification is less secure. However, none of the power laws we fit in these sources contradict the high power law indices found in sources with higher signal to noise.

4.1 Precession due to frame dragging

4.1.1 Test particle

Frequencies compatible with Lense-Thirring (LT) precession due to frame dragging of a test particle orbit as proposed by [Stella & Vietri \(1998\)](#) are not in correspondence to our findings, as the correlations to ν_u traced out by the candidate ν_{LT} frequencies (ν_h , ν_{LF} and ν_b) mostly have power law indices significantly higher than 2. For this reason, the relativistic precession model in its original form is incompatible with our data.

As noted previously ([Stella & Vietri 1998](#); [van Straaten et al. 2003](#)) the observed frequencies also tend to be higher than predicted for acceptable values of I/M . Figure 16 shows the range of possible relativistic precession frequencies ν_{LT} vs. spin frequency together with our measurements of ν_b , ν_{LF} and ν_h at $\nu_u = 600$ Hz. Realistic equations of state limit the value of I_{45}/m to a maximum of 2 and a minimum of 0.5 (*hatched region* in the Figure; [Stella & Vietri 1998](#); [Friedman et al. 1986](#); [Cook et al. 1994](#)) which is still well below the I_{45}/m required by our measured ν_h , and also below ν_{LF} for five out of nine sources. Remarkably, all our measured ν_b fit this prediction. If we assume the observed frequencies are twice the precession frequency (*yellow region*), which is not unrealistic ([Stella & Vietri 1998](#)), the model predictions are in the observed ν_{LF} range, but still below ν_h in four out

of eight sources. A dependence of the precession frequency on spin is not evident in our data.

A latitude dependent radiation field as proposed by [Miller \(1999\)](#) can increase the test particle precession frequency significantly, even in low luminosity sources. Radiation forces could possibly affect the index of a power law correlation between the precession frequency and ν_K as they are strongest for small radii, and have a much smaller effect on orbital frequencies. We note that [Miller \(1999\)](#) argues that narrow QPOs are hard to form via precession when including radiation forces. Asymmetry in the radiation field for instance would increase the FWHM of the QPO significantly.

4.1.2 Torus

The model of [Ingram et al. \(2009\)](#) describes the inner accretion flow as a torus characterized by an inner and outer radius that precesses as a solid body due to frame dragging. Outside the outer radius of the torus is the thin disk. In [Ingram & Done \(2010\)](#) the authors propose that the frequencies of broad components L_b and L_{hHz} in NS-LMXBs represent the viscous timescales at the outer and inner radius, respectively. The emergence of L_{b2} for $\nu_u > \sim 700$ Hz is explained by the disk moving inward, penetrating the hot flow. L_{b2} then tracks the viscous timescale in the overlap region. By parametrizing the viscous timescale, the inner and outer radius of the torus can be obtained from the measured frequencies. The nodal precession frequency of the torus ($\nu_{LT,t}$) is a mass-weighted average of Lense-Thirring precession frequencies at different radii in the torus, and is proposed to be associated with ν_{LF} . What mechanism sets ν_h has not been specified in this model.

As the disk moves in, it is possible that the torus narrows, so its mass can effectively become increasingly concentrated towards the inner radius, favoring progressively higher precession frequencies. In this way, identifying ν_u with the orbital frequency ν_K at the inner disk edge outside the torus, a $\nu_{LT,t}$ - ν_K correlation with a power law index higher than 2 might be obtained. As the precession frequency originates closer to the neutron star than ν_u , lower values of I/M are required to match the data, so that I/M is closer to the range predicted for realistic equations of state. We note that for high ν_u , when we presume the torus to be narrower, fewer radii contribute to the precession frequency, and the test particle case is approximately recovered. So probably this interpretation still requires $\nu_{LF} = 2\nu_{LT,t}$ for the predicted $\nu_{LT,t}$ to match the data at high ν_u for realistic I/M . This could also explain a possible decrease of the power law index toward higher ν_u which, however, only in 4U 1728–34 we can detect significantly, see Section 3.1.5 and Table 3, as well as the fact that the index significantly exceeds 2.0 even at the highest frequencies.

4.2 Classical and magnetic precession

[Altamirano et al. \(2012\)](#) found that in the 11 Hz pulsar IGR J17480–2446, the LF-QPO (35–50 Hz) cannot be caused by frame dragging, which is prograde with respect to the spin. They suggest that the LF-QPO might be mainly attributable to retrograde classical and magnetic precession. These additional torques are expected to operate on the disk

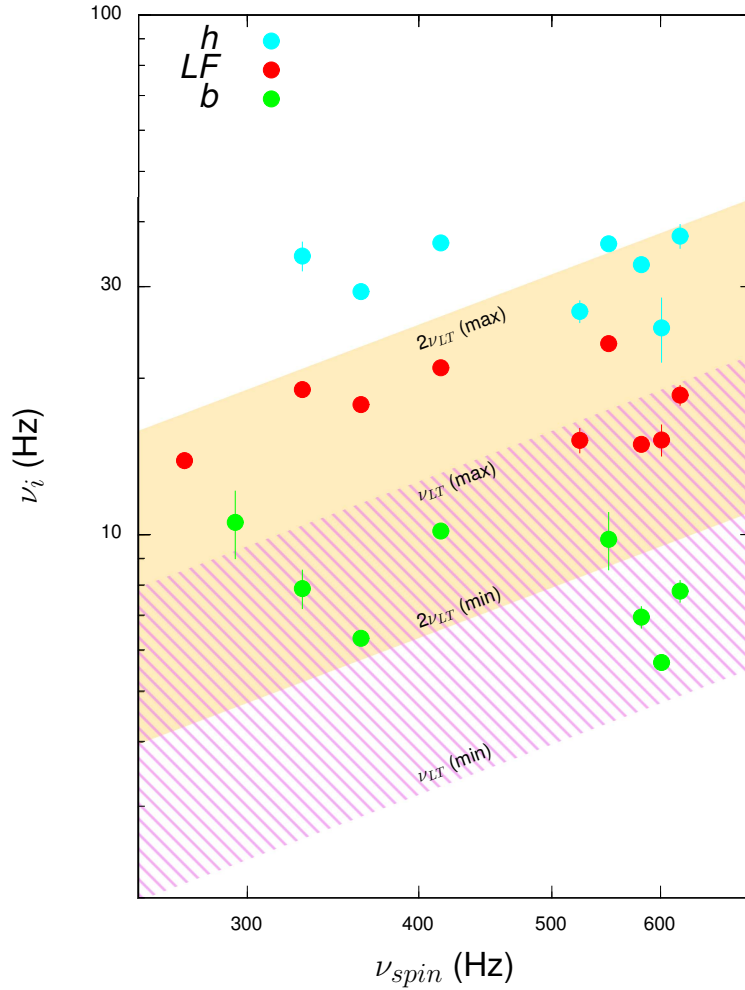


Figure 16. Frequencies ν_b , ν_{LF} and ν_h for each source corresponding to $\nu_u=600$ Hz vs. spin frequency, plotted with ν_{LT} model predictions, see text.

around a neutron star due to magnetic stresses and stellar oblateness. If the magnetic field axis does not coincide with the spin axis of the neutron star, which is the case for pulsars, the magnetic torque causes misalignment of the disk angular momentum with the spin axis of the neutron star and drives magnetic precession (with frequency ν_m). Stellar oblateness causes classical precession with frequency ν_{cl} (Morsink & Stella 1999; Shirakawa & Lai 2002). The three precessional effects depend differently on radius and hence on Keplerian orbital frequency; $\nu_{LT} \propto \nu_K^2$, $\nu_m \propto -(\nu_K^{14/3})$, $\nu_{cl} \propto -(\nu_K^{7/3})$. Depending on the coupling mechanism between different radii in the accretion disk and the amount of warping, a net overall precession frequency can arise from the combination of these three torques. Depending on the system parameters, either the prograde (frame dragging) or the retrograde (magnetic and classical) precession will dominate. Adopting a realistic parameter set for a weakly magnetized ($B \sim 10^8$ G) neutron star, taking into account all three precession effects as well as warping, Shirakawa & Lai (2002) predict a prograde precession frequency that correlates with the Keplerian orbital frequency according to a power law with an index below 2 (no exact number is given). Increasing

the warping or the magnetic dipole moment lowers the index of the correlation even further. So, the high power law indices of the correlations we measure cannot be explained by adding classical and magnetic precession effects to (dominant) Lense-Thirring precession.

If instead the system parameters would be such that (retrograde) magnetic precession dominates, a much steeper power law index may be obtained as $\nu_m \propto -(\nu_K^{14/3})$. The observational result of Bult & van der Klis (2015b), where the 410 Hz QPO in the 401 Hz AMXP SAX J1808.4–3658 is explained as a beat of the spin frequency with a retrograde precession frequency would support this scenario.

Our observational results are incompatible with frame-dragging induced precession taking place at test particle frequencies. However, they may be explained in the scenario where the entire inner flow precesses due to frame dragging, in which case multiple radii (with variable weighting) are expected to contribute to the precession frequency (Ingram et al. 2009). Since a variety of torques are expected around neutron stars, if a QPO is produced by precession, frame dragging is likely only one of the torques contributing to that precession. In any case, unless differential precession

(van den Eijnden et al. 2016) affects different harmonics unequally, precession can only explain the occurrence of one frequency, while we observe three QPOs in the ν_{LT} range with no strong evidence for integer frequency ratios. In black holes as well, then, LF QPO frequencies might be expected to differ from test-particle Lense-Thirring values. This is in accordance with recent findings on the iron line modulation with QPO phase in the black hole H 1743–322 which suggest that a precessing torus produces the LF-QPO in that system (Ingram et al. 2016).

5 ACKNOWLEDGEMENTS

This research has made use of data obtained through the High Energy Astrophysics Science Archive Research Center Online Service, provided by the NASA/Goddard Space Flight Center. This work is (partly) financed by the Netherlands Organisation for Scientific Research (NWO). M. van Doesburgh thanks Peter Bult, Diego Altamirano and Adam Ingram for many useful discussions. We thank the referee for the constructive feedback and suggestions that improved the quality of the paper.

REFERENCES

- Altamirano D., van der Klis M., Méndez M., Jonker P. G., Klein-Wolt M., Lewin W. H. G., 2008, *ApJ*, **685**, 436
- Altamirano D., Ingram A., van der Klis M., Wijnands R., Linares M., Homan J., 2012, *ApJ*, **759**, L20
- Belloni T., Psaltis D., van der Klis M., 2002, *ApJ*, **572**, 392
- Bult P., van der Klis M., 2015a, *ApJ*, **798**, L29
- Bult P., van der Klis M., 2015b, *ApJ*, **806**, 90
- Casella P., Altamirano D., Patruno A., Wijnands R., van der Klis M., 2008, *ApJ*, **674**, L41
- Cook G. B., Shapiro S. L., Teukolsky S. A., 1994, *ApJ*, **422**, 227
- Di Salvo T., Méndez M., van der Klis M., Ford E., Robba N. R., 2001, *ApJ*, **546**, 1107
- Ford E. C., van der Klis M., 1998, *ApJ*, **506**, L39
- Friedman J. L., Ipser J. R., Parker L., 1986, *ApJ*, **304**, 115
- Hasinger G., van der Klis M., 1989, *A&A*, **225**, 79
- Ingram A., Done C., 2010, *MNRAS*, **405**, 2447
- Ingram A., Done C., Fragile P. C., 2009, *MNRAS*, **397**, L101
- Ingram A., van der Klis M., Middleton M., Done C., Altamirano D., Heil L., Uttley P., Axelsson M., 2016, *MNRAS*, **461**, 1967
- Klein-Wolt M., 2004, PhD thesis, University of Amsterdam
- Klein-Wolt M., van der Klis M., 2008, *ApJ*, **675**, 1407
- Miller M. C., 1999, *ApJ*, **520**, 256
- Morsink S. M., Stella L., 1999, *ApJ*, **513**, 827
- Motta S. E., Belloni T. M., Stella L., Muñoz-Darias T., Fender R., 2014, *MNRAS*, **437**, 2554
- Nowak M. A., 2000, *MNRAS*, **318**, 361
- Patruno A., Watts A. L., 2012, preprint, ([arXiv:1206.2727](https://arxiv.org/abs/1206.2727))
- Press W. H., Teukolsky S. A., Vetterling W. T., Flannery B. P., 1992, Numerical recipes in FORTRAN. The art of scientific computing
- Psaltis D., Belloni T., van der Klis M., 1999, *ApJ*, **520**, 262
- Ritter H., Kolb U., 2003, *A&A*, **404**, 301
- Shirakawa A., Lai D., 2002, *ApJ*, **565**, 1134
- Stella L., Vietri M., 1998, *ApJ*, **492**, L59
- Strohmayer T. E., Markwardt C. B., 2002, *ApJ*, **577**, 337
- Watts A. L., 2012, *ARA&A*, **50**, 609
- Wijnands R., van der Klis M., 1999, *ApJ*, **514**, 939
- Zhang W., Jahoda K., Swank J. H., Morgan E. H., Giles A. B., 1995, *ApJ*, **449**, 930
- van Straaten S., Ford E. C., van der Klis M., Méndez M., Kaaret P., 2000, *ApJ*, **540**, 1049
- van Straaten S., van der Klis M., di Salvo T., Belloni T., 2002, *ApJ*, **568**, 912
- van Straaten S., van der Klis M., Méndez M., 2003, *ApJ*, **596**, 1155
- van Straaten S., van der Klis M., Wijnands R., 2005, *ApJ*, **619**, 455
- van den Eijnden J., Ingram A., Uttley P., 2016, *MNRAS*, **458**, 3655
- van der Klis M., 1989, in Ögelman H., van den Heuvel E. P. J., eds, NATO Advanced Science Institutes (ASI) Series C Vol. 262, NATO Advanced Science Institutes (ASI) Series C. p. 27
- van der Klis M., 2006, Rapid X-ray Variability. pp 39–112

APPENDIX A: MAP FITTING

Standard χ^2 methods for performing the power-law fits to our frequency correlations run into a number of problems.

First, the data have error bars in both coordinates (v_u and v_x , where x is b , LF or h) which means that for arbitrary fit functions a well-behaved χ^2 statistic taking into account both errors must be defined.

Second, the frequency measurements are obtained by performing multi-Lorentzian model fits to power spectra with typically 15–24 free parameters. Such fits typically result in asymmetric error bars, the interpretation of which, in terms of the contribution to the χ^2 statistic made by a data point depending on whether the fit function passes it on the side of the larger or the smaller error bar, is uncertain, as the information about the actual probability distribution of the parameter is not preserved in the ‘error-bar’ description.

Third, although in our case this was usually not the case, such fits can result in strongly correlated errors, biasing any true correlation between the two frequencies fitted.

We resolved these issues by employing a method that is mathematically identical to performing a joint fit to all power spectra simultaneously, with all multi-Lorentzian parameters free except that the two frequencies of interest are tied together by the power law relation we desire to fit. The power law parameters act as two more fit parameters added to the total set of fit parameters. For a typical power-law fit to 100 frequency pairs this entails a simultaneous fit to 100 power spectra with typically 2000 free parameters and 40000 *dof*, which would be unwieldy to perform directly.

We therefore performed the fit in two steps. In the first step, we fit each individual power spectrum with the multi-Lorentzian model, and perform a scan of the χ^2 values in the v_u , v_x plane around the best fit, leaving all other parameters free to minimize χ^2 in the usual way (e.g., Press et al. 1992). The resulting χ^2 maps, one for each power spectrum, form the input to the second step, the power law fit.

In the second step, we fit a power law to all the χ^2 maps in the v_u , v_x diagram by varying the two power law parameters and minimizing the total χ^2 of the power law fit. This total χ^2 is defined as the sum of the χ^2 contributions of each map, where each map’s contribution is just the lowest χ^2 value in the map corresponding to a point on the power law (see Figure A1).

A difficulty that had to be overcome in applying this procedure is that sometimes the trial power law runs so far from a χ^2 map center, that the implied v_u , v_x pairs can not fit the power spectrum, as one or both frequencies come too close to other features in the power spectrum than the ones identified as L_u and L_x , which results in an altogether different multi-Lorentzian fit where the fitted frequencies no longer represent the intended power spectral components. In terms of the χ^2 maps, this translates in a secondary minimum in χ^2 . To overcome this problem, we truncated our map scans before the turn-over to the secondary minimum, and when necessary extrapolated the maps using an elliptical paraboloid extrapolation scheme. So, in cases where the power law runs far from a map center we conservatively assign a larger χ^2 contribution to that map than that corresponding to the statistically ‘best’ (but physically incorrect) fit, a contribution that is representative of the χ^2 that the map would have contributed if the L_u and L_x components

Source	L_b false/tot.	L_{LF} false/tot.	L_h false/tot.	L_u false/tot.
4U 1728–34	1.38/165	1.53/148	1.10/118	0.35/188
4U 0614+09	0.81/97	2.15/76	1.05/55	0.34/136
4U 1608–52	0.04/27	0.23/16	0.21/16	0.55/31
4U 1636–53	0.22/35	0.64/27	0.27/25	0.06/38
4U 1702–43	0.38/21	0.56/16	0.02/12	0.03/24
Aquila X-1	0.05/22	0.47/16	0.26/29	0.08/34
SAX J1750–2900	0.03/6	0.01/3	0.01/4	0.03/6
4U 1915–05	0.18/3	0.05/16	-	0.05/15
KS 1731–260	0.01/7	0.54/10	0.01/11	0.01/11
IGR J17191–2821	0.20/5	-	-	0.03/5

Table B1. Expected false positives out of the total number of fitted Lorentzians per source.

in the fit function would have been forced to continue to describe their intended counterparts in the observed power spectra. In practice, for all our final power law fits, <20% of maps were extrapolated (8, 12, and 20% for L_{LF} , L_h and L_b , respectively).

We offer a comparison of this method to the result we obtain when minimizing χ^2 with a standard fitting routine in which only vertical errors are taken into account. We use the v_{LF} of Group 2 in 4U 1728–34 with 133 frequency measurements here. With the standard method we obtain a best-fit with normalization $1.37(\pm 0.06) \times 10^{-6}$ and power law index 2.56 ± 0.01 , with χ^2/dof : 1689/131. The best fit with the map fitting technique gives a normalization of $2.42(\pm 0.20) \times 10^{-6}$, a power law index of $2.47(\pm 0.01)$ and χ^2/dof : 45677/43389.

APPENDIX B: DETECTION SIGNIFICANCE OF QPOS

We report all fitted Lorentzians that were needed to characterize power spectra and include all centroid frequencies in our power law fits except in cases noted below. As we are able to track components over different observations, we are able to usefully include centroid frequencies of Lorentzians detected at significance levels $<3\sigma$ (down to 2σ , calculated from the negative error on the integral power of the Lorentzian). We do this only if the component is detected at $>3\sigma$ in similar observations. In Table B1 we quote the expected number of false positives for L_b , L_{LF} , L_h and L_u resulting from the ensemble of detection significances for each component in each source. Clearly these numbers are very small.

APPENDIX C: DETAILED RESULTS FOR INDIVIDUAL SOURCES

In this appendix we present some details on the results obtained for the individual sources in our sample. For each source separately we display the measured frequencies vs. v_u as in Figure 2, with the best-fit power laws (*dashed*) to Group 2 as specified in Table C3. All power spectral fit parameters can be found in Table C2; the full version is available online. The power law fit results can be found in Table 3. For selected sources we also display fractional rms and Q values similarly to Figures 6 and 7.

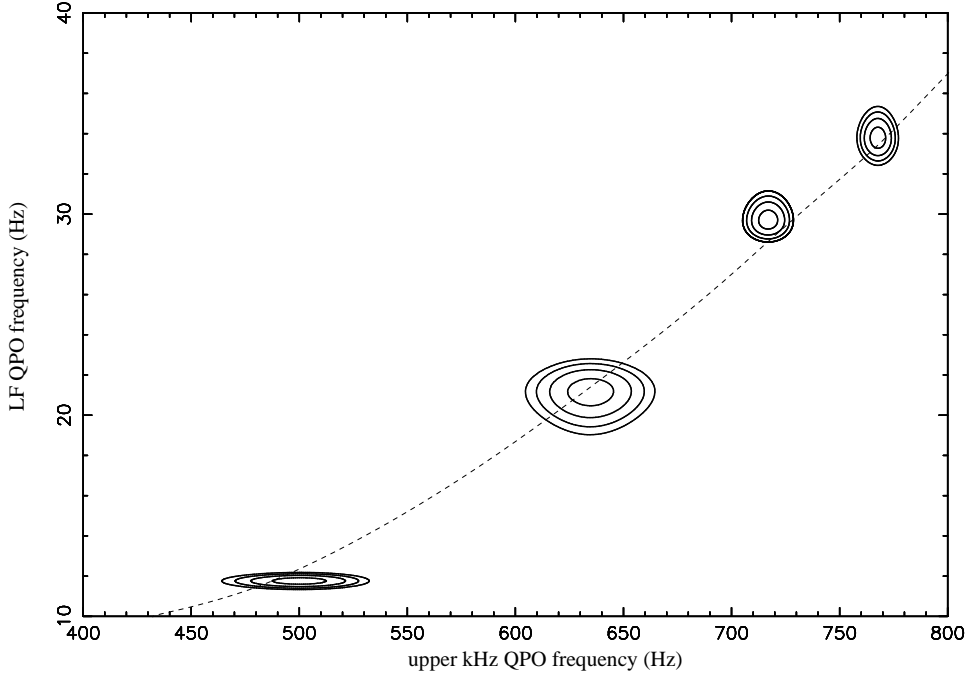


Figure A1. Example of a power law fit to χ^2 maps of ν_{LF} - ν_u frequency pairs. Shown are the $\Delta\chi^2=1,3,5$ and 7 contours of a selection of measured frequency pairs from Group 2 of 4U 1728–34 as well as the best-fit power law (*dashed line*).

Source	Row A	Row B	Row C	Row D	High ν_u
4U 1728–34	30042-03-18-00	50023-01-25-00	50023-01-30-00	20083-01-04-00	20083-01-02-000/01
4U 0614+09	50031-01-04-13	30053-01-03-01/02	20074-01-07-00	80037-01-06-00	40030-01-06-00
4U 1608–52	30062-02-02-00/000	60052-03-01-00/01	60052-02-06/07-00	30062-02-01-000	-
4U 1636–53	92023-01/02-11-00	60032-05-10-00/000	60032-05-07-00/01	60032-01-06-00/000	-
4U 1702–43	50030-01-04-00/000	80033-01-18-01/02/03	40025-04-03-01	X-06-01/02 and X-04-04	X-10-03, X-15-01, X-12-05, X-12-04, X-14-05, X-15-02, X-11-00, X-14-06, X-10-01, X-10-02
Aquila X-1	91414-01-08-05/06	60054-02-02-02	90017-01-09-02	50049-02-15-05/06	30188-03-01-00

Table C1. The observations we used to make the power spectra shown in Figures 4, 5 and 10. Observations “20083-01-02-000/01” for instance means we included both 20083-01-02-000 and 20083-01-02-01, “X” stands for “80033-01”.

C1 4U 1728–34

For $\nu_u > 700$ Hz, the ν_{LF} - ν_u correlation in 4U 1728–34 slightly flattens (see Figure C1), as also reflected in a lower power law index of the best-fit power law to the ν_{LF} - ν_u frequency pairs when combining Groups 2 and 3, and when fitting ν_{LF} in Group 2 above $\nu_u = 600$ Hz, see Table 3. When including ν_{LF} when $\nu_u > 700$ Hz (with ν_{LF} in Group 2 and 3), we obtain a best-fit power law index of $2.13^{+0.05}_{-0.04}$, which is still in excess of 2.0 at 3.2σ .

Comparing the low signal to noise power spectra of 91023-01-02-00, 92023-03-41-00, 92023-03-57-00, and 92023-03-82-00 all with $\nu_u \sim 1100$ Hz, to high signal to noise power spectra with similar colours, we conclude that the single fitted Lorentzian at low frequency is a blend of L_b and L_{b_2} . We designate this blend L_b in Table C2 and (by plotting colour) in the figures although it is broader than L_b fitted in high signal to noise power spectra and its centroid frequency does not fall on the extrapolation of the ν_b - ν_u correlation for $\nu_u < 1000$

Hz. In 40033-06-03-04, L_h with $\nu_h \sim 41$ Hz can only be fitted when fixing the width.

C2 4U 0614+09

The timing behaviour of 4U 0614+09 strongly resembles that of 4U 1728–34 both in terms of frequencies and rms (compare Figures C3 and C1, and Figures C4 and C2, respectively), but the flattening of the ν_h - ν_u and ν_{LF} - ν_u correlations at $\nu_u < 400$ Hz in 4U 1728–34, is not evident in 4U 0614+09. We test whether the power law index changes as ν_u increases (see Table 3 for ν_{LF} within Group 2). When $\nu_u > 700$ Hz, including ν_{LF} in Group 2 and 3, the best-fit power law has index 2.18 ± 0.05 , which is still significantly in excess of 2.0 at 3.8σ . The data point with ν_l at 205 Hz when $\nu_u \sim 600$ Hz that falls below the ν_l - ν_u correlation corresponds to a 2.5σ detection in 91425-01-03-00. By an F-test this component is required at the 3.5σ level. We detect a 4σ

Source	ObsID	No. of obs.	No. of power spectra	ν (Hz)	L_b	L_{LF}	L_h	L_u	IP ($\times 10^{-3}$)	ν (Hz)	FWHM (Hz)	I_u	IP ($\times 10^{-3}$)	χ^2/dof		
4U 1728-34	50030-03-05-02	1	629	0.30 \pm 0.05	1.80 $^{+0.10}_{-0.09}$	15.5 $^{+0.6}_{-0.6}$	2.93 $^{+0.13}_{-0.09}$	0.55 $^{+0.49}_{-0.31}$	0.40 $^{+0.34}_{-0.20}$	5.35 $^{+0.18}_{-0.16}$	6.99 $^{+0.52}_{-0.46}$	17.6 $^{+1.5}_{-1.0}$	183.3 $^{+27.0}_{-17.4}$	327.4 $^{+66.8}_{-51.7}$	16.9 $^{+2.6}_{-2.2}$	341.98/327
	30042-03-01-01	2	264	0.27 $^{+0.06}_{-0.05}$	2.01 $^{+0.13}_{-0.12}$	15.5 \pm 0.6	3.20 $^{+0.08}_{-0.08}$	0.46 $^{+0.30}_{-0.27}$	0.32 $^{+0.18}_{-0.18}$	5.34 $^{+0.18}_{-0.18}$	6.96 $^{+0.49}_{-0.49}$	17.2 $^{+1.5}_{-1.5}$	200.5 $^{+17.4}_{-17.4}$	380.8 $^{+45.7}_{-45.7}$	15.9 $^{+1.3}_{-1.1}$	312.54/327
	30042-03-18-00	1	589	0.34 $^{+0.08}_{-0.08}$	2.50 \pm 0.10	17.0 \pm 0.4	4.00 \pm 0.06	1.40 $^{+0.27}_{-0.27}$	1.58 $^{+0.38}_{-0.38}$	7.84 $^{+0.46}_{-0.46}$	8.16 $^{+0.81}_{-0.81}$	12.7 $^{+2.4}_{-2.4}$	203.0 $^{+18.6}_{-18.6}$	450.4 $^{+33.7}_{-33.7}$	19.5 $^{+1.2}_{-1.2}$	332.89/324
	30042-03-20-00	1	257	0.31 $^{+0.08}_{-0.08}$	2.44 $^{+0.14}_{-0.14}$	16.5 \pm 0.7	3.82 $^{+0.11}_{-0.11}$	1.27 $^{+0.39}_{-0.36}$	1.26 $^{+0.63}_{-0.63}$	7.29 $^{+0.54}_{-0.54}$	7.88 $^{+0.86}_{-0.86}$	14.5 $^{+3.1}_{-3.1}$	225.0 $^{+24.2}_{-24.2}$	367.0 $^{+47.7}_{-47.7}$	15.1 $^{+1.3}_{-1.3}$	364.60/324
	30042-03-04-00	1	410	0.28 $^{+0.06}_{-0.07}$	2.20 $^{+0.11}_{-0.11}$	16.4 \pm 0.7	3.42 $^{+0.04}_{-0.04}$	0.77 $^{+0.15}_{-0.15}$	1.23 $^{+0.23}_{-0.23}$	6.90 $^{+0.28}_{-0.28}$	6.31 $^{+0.86}_{-0.86}$	9.5 $^{+2.8}_{-2.8}$	226.1 $^{+29.6}_{-29.6}$	406.3 $^{+47.7}_{-47.7}$	14.5 $^{+1.3}_{-1.3}$	336.18/322
	30042-03-01-02	2	229	0.48 \pm 0.04	1.63 $^{+0.17}_{-0.17}$	12.7 \pm 1.4	3.19 $^{+0.06}_{-0.06}$	0.91 $^{+0.22}_{-0.22}$	1.29 $^{+0.40}_{-0.40}$	6.93 $^{+0.18}_{-0.18}$	4.57 $^{+1.16}_{-1.16}$	4.7 $^{+5.4}_{-2.0}$	253.1 $^{+27.3}_{-27.3}$	319.4 $^{+54.9}_{-54.9}$	11.1 $^{+2.7}_{-2.7}$	368.50/322
	30042-03-01-04	1	206	0.37 $^{+0.05}_{-0.06}$	1.84 $^{+0.13}_{-0.12}$	15.5 \pm 0.7	3.15 $^{+0.10}_{-0.10}$	0.91 $^{+0.48}_{-0.48}$	0.88 $^{+0.58}_{-0.58}$	5.58 $^{+0.33}_{-0.33}$	7.10 \pm 0.46	16.9 \pm 1.8	275.3 $^{+12.2}_{-12.2}$	261.2 $^{+31.9}_{-31.9}$	10.7 $^{+1.0}_{-1.0}$	338.86/324
	40033-06-01-00	1	589	0.30 \pm 0.06	2.59 \pm 0.10	16.6 \pm 0.5	4.08 \pm 0.06	1.18 $^{+0.27}_{-0.27}$	1.22 $^{+0.32}_{-0.32}$	7.48 $^{+0.31}_{-0.31}$	8.52 \pm 0.57	14.9 $^{+1.6}_{-1.6}$	325.5 $^{+13.4}_{-13.4}$	229.9 $^{+36.1}_{-36.1}$	9.4 $^{+1.3}_{-1.3}$	307.31/321
	30042-03-03-01	1	276	0.38 $^{+0.06}_{-0.06}$	1.89 \pm 0.15	15.1 \pm 0.8	3.13 $^{+0.10}_{-0.10}$	1.95 $^{+0.25}_{-0.25}$	3.03 $^{+0.80}_{-0.80}$	6.79 $^{+1.07}_{-1.07}$	6.89 $^{+1.07}_{-1.07}$	13.3 $^{+4.3}_{-4.3}$	331.1 $^{+30.6}_{-30.6}$	249.7 $^{+35.2}_{-35.2}$	9.1 $^{+1.9}_{-1.9}$	338.31/320
	30042-03-06-00	1	540	0.37 \pm 0.05	2.40 $^{+0.11}_{-0.10}$	15.5 \pm 0.4	3.86 $^{+0.06}_{-0.07}$	1.65 $^{+0.29}_{-0.25}$	1.96 $^{+0.33}_{-0.35}$	7.65 $^{+0.42}_{-0.42}$	7.73 $^{+0.60}_{-0.63}$	12.2 \pm 2.0	333.1 $^{+13.4}_{-13.6}$	244.7 $^{+33.8}_{-34.4}$	9.1 $^{+1.3}_{-1.7}$	408.32/321

Table C2: Shortened table with parameters of the multi-Lorentzian fits per source. The number of averaged subsequent observations and power spectra are given in columns 3 and 4, respectively. We quote the centroid frequency (ν), full width at half maximum (FWHM) and rms-normalized integral power (IP) of L_b , L_{LF} , L_h and L_u . The quoted errors use $\Delta\chi^2=1$. The full version, with all parameters for all sources, is available online.

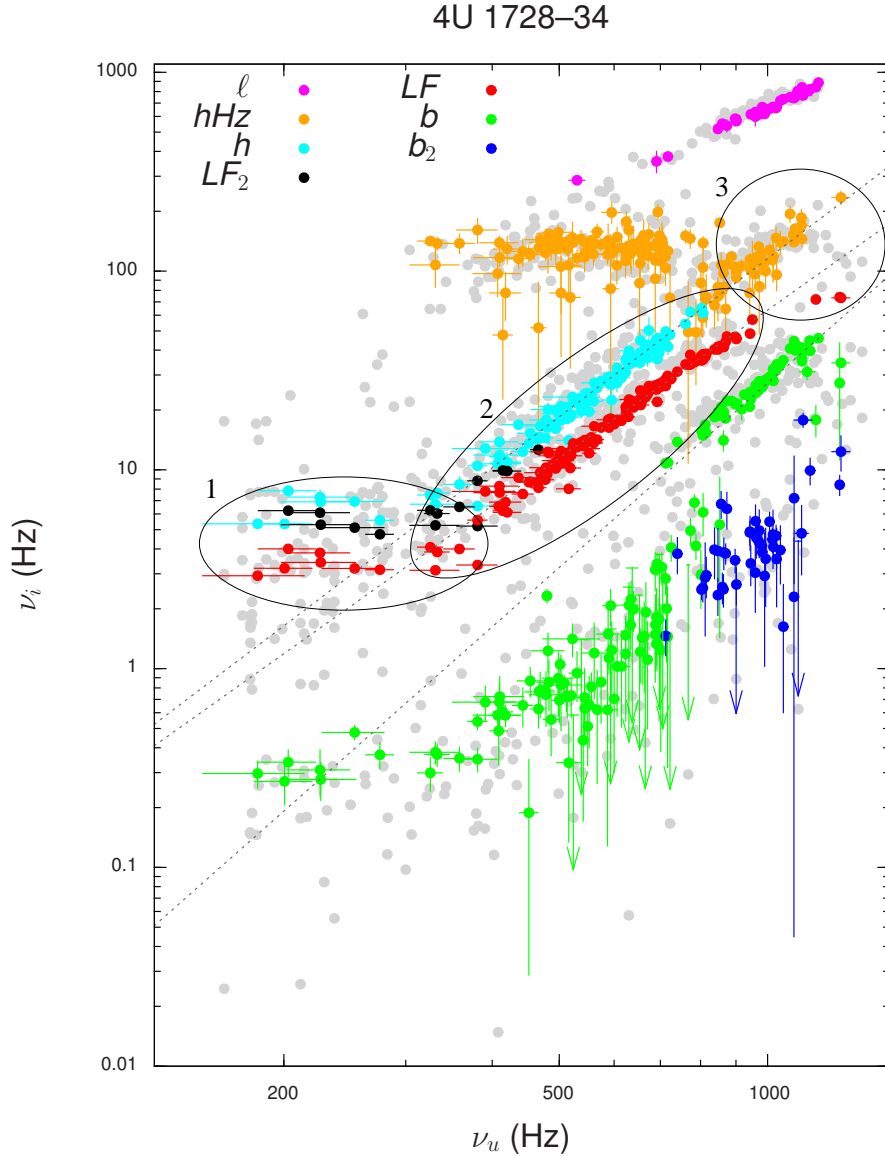


Figure C1. As in Figure 2, but for 4U 1728–34. Best-fit power laws to ν_h and ν_{LF} in Group 2 are shown, as well as to ν_b for data with $Q_b > 0.5$. The identification of the ν_{LF} data in Group 3 (red) is tentative. Frequencies measured in all other sources in our sample are plotted in grey.

110 Hz feature in the same power spectrum, which supports our identification of the 205 Hz feature as ν_ℓ and not ν_{hHz} .

At $\nu_u \sim 400$ Hz, the ν_h data fall below the correlation traced out for $\nu_u > 500$ Hz. We fail to significantly detect L_{LF_2} in these power spectra, but do detect a power excess at $\sim 2\nu_{LF}$, suggesting that the lower ν_h might be a result of blending of L_h and L_{LF_2} (this refers to observations: 50031-01-01-01/02/03/07/08/09, 50031-01-02-01/09, 50031-01-03-01/03/07/08, 50031-01-04-13).

In 10073-01-10-01 (with $\nu_u \sim 380$ Hz) Q_u is high (> 1.5) which is atypical for Group 1, we therefore add ν_{LF} and ν_h to Group 2.

C3 4U 1608–53

Although with fewer data points, the timing behaviour of 4U 1608–53 is similar to that of 4U 1728–34, although we do not detect L_{LF} for $\nu_u > 500$ Hz (see Figures C1, C5 and C6).

C4 4U 1636–52

The data of 4U 1636–52 contain many short observations, and as the source is not bright we can by our selection criteria (which do not allow to combine data over wide time spans) only use a small fraction of the available data. As previously noted by Altamirano et al. (2008), this source behaves similarly to 4U 1728–34, 4U 0614+09 and 4U 1608–53 (for instance, compare Figures C7 and C1). In 95087-01-50-

Source	Group	Range of ν_u (Hz) L_{LF}	Range of ν_u (Hz) L_h
4U 1728–34	1	<381	<381
	2	381–950	381–806
	3	>950	>806
4U 0614+09	1	-	-
	2	<872	<872
	3	>872	>872
4U 1608–52	1	<215	<215
	2	215–531	215–531
	3	-	>531
4U 1636–53	1	-	-
	2	<772	<910
	3	>772	-
4U 1702–43	1	-	-
	2	<888	<542
	3	>888	>542
Aquila X-1	1	-	-
	2	<973	<761
	3	>973	>761

Table C3. Specifications of frequency ranges defining groups of data points in the frequency-frequency plots used to fit power laws. In Group 3 we take ν_{hHz} as ν_h only if L_{hHz} and L_h are not detected in the same power spectrum.

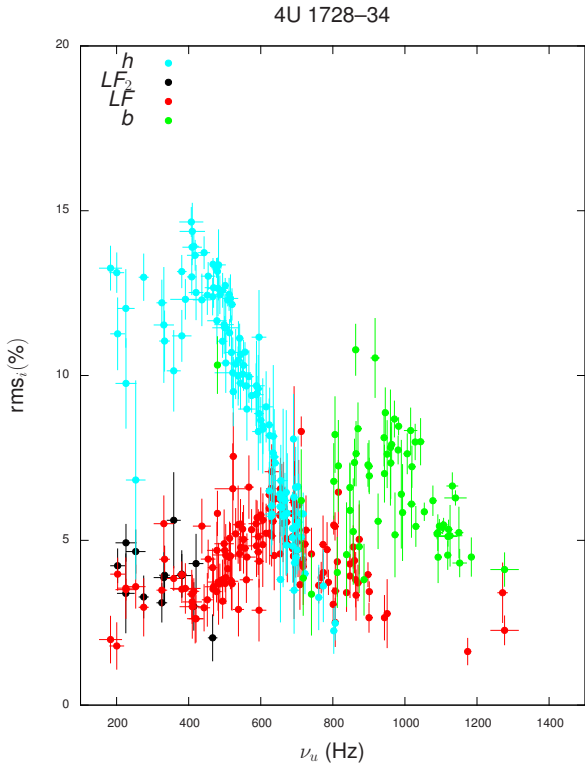


Figure C2. Fractional rms levels of Lorentzians vs. ν_u in 4U 1728–34. We only plot rms_b for $Q_b > 0.5$

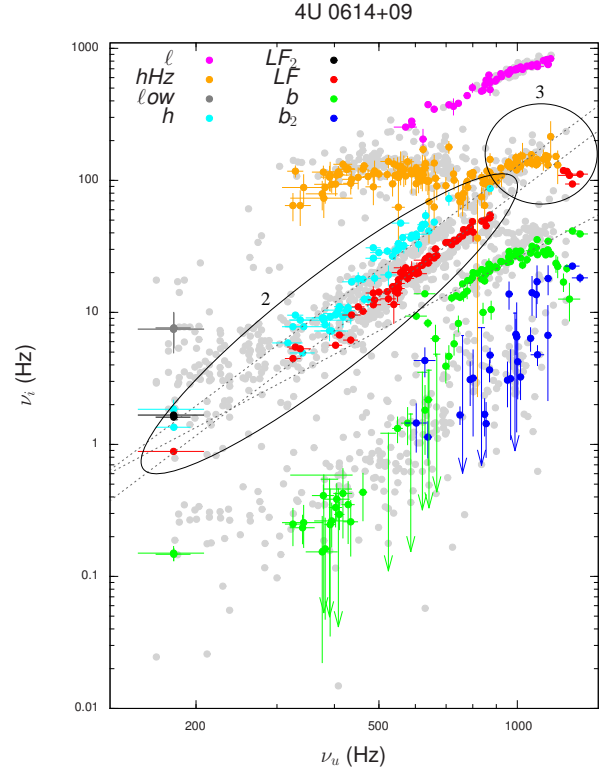


Figure C3. Same as Figure C1; but for 4U 0614+09.

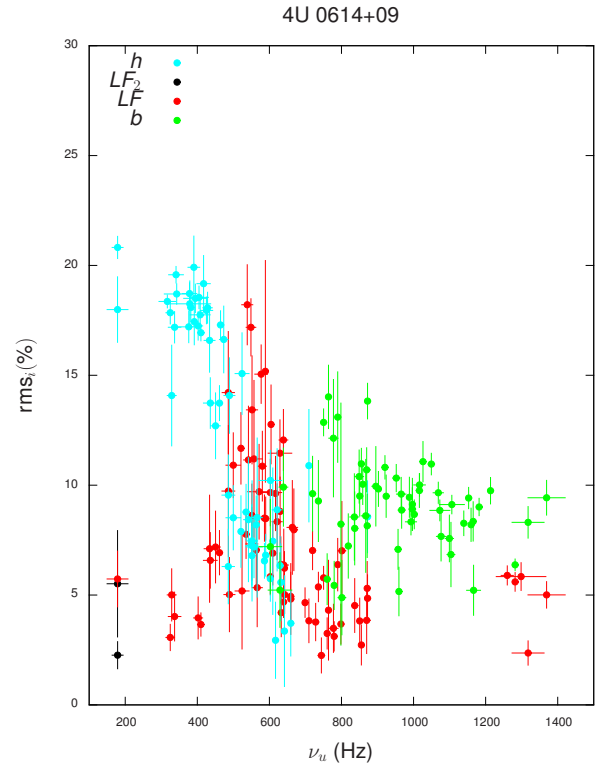


Figure C4. Same as Figure C2; but for 4U 0614+09.

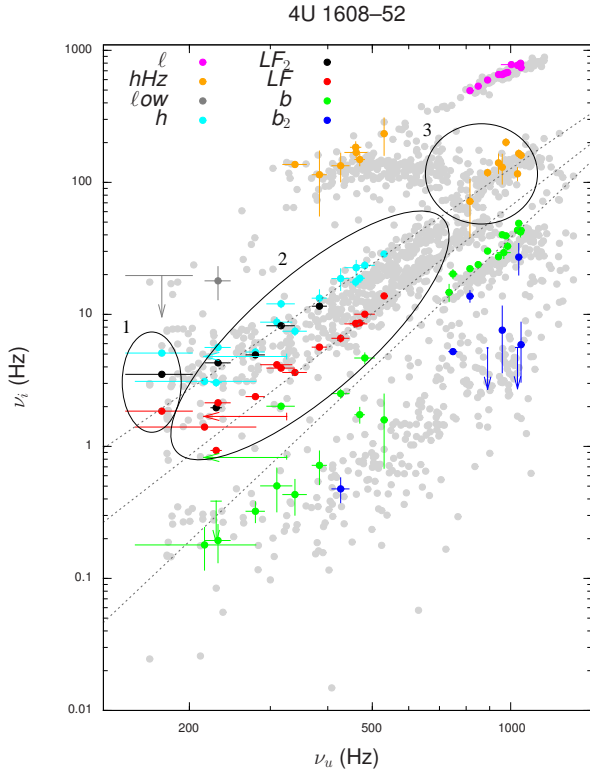


Figure C5. Same as Figure C1; but for 4U 1608-52.

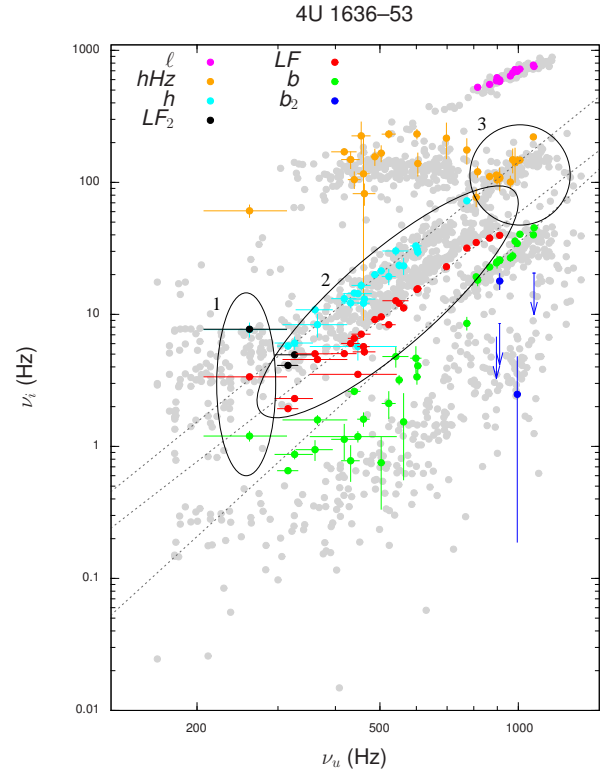


Figure C7. Same as Figure C1; but for 4U 1636-53.

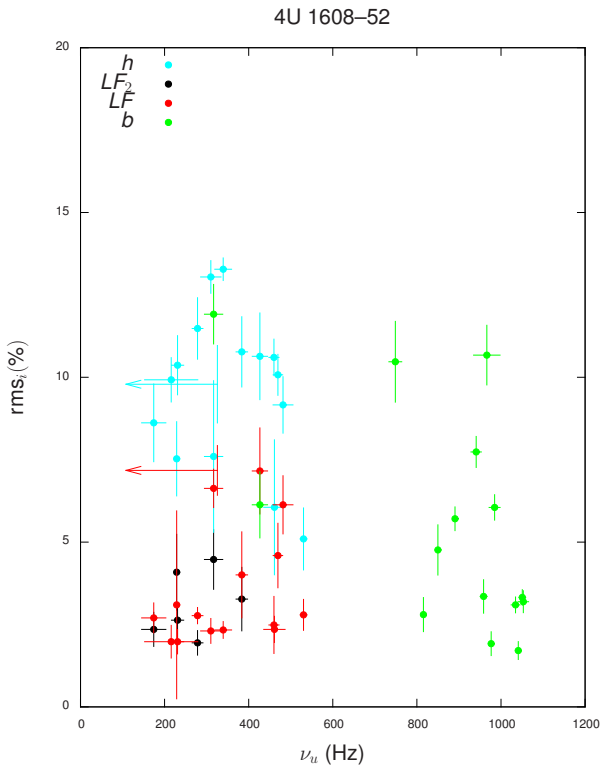


Figure C6. Same as Figure C2; but for 4U 1608-52.

10 we fit a broad zero-centered Lorentzian where, based on other data with similar colours (e.g. 91024-01-75-00), one would expect a kHz QPO with a frequency around 366 Hz. As this may indicate that the features moved during the observation, we discarded this power spectrum from our analysis. In 92023-01-02-10, L_h and L_{LF} are characterized by unusually low centroid frequencies ($\nu_u \sim 450$ Hz). Apart from the low ν_h and ν_{LF} this power spectrum is very similar to that of, e.g., 80425-01-04-02 supporting our identification of these features. We therefore include these frequencies in our frequency-frequency correlation fitting.

C5 4U 1702-43

In 4U 1702-43, we do not see a flattening of the frequency correlations at low ν_u (see Figure C8). We therefore do not define a frequency Group 1.

C6 Aquila X-1

The power spectra of Aquila X-1 closely resemble those of the other sources in our sample. For the identification of L_h , L_{LF} and L_{LF_2} we use Figures C10 and C11. The upper kHz QPO at low frequencies is very broad, which explains the structure of the frequency-frequency plot below $\nu_u = 300$ Hz, see Figure C9.

In 40049-01-02-02 at $\nu_u \sim 200$ Hz, we fit an unusually broad L_{LF} as compared to other power spectra with similar colours, and a narrow L_h (see Figure C10). We consider the

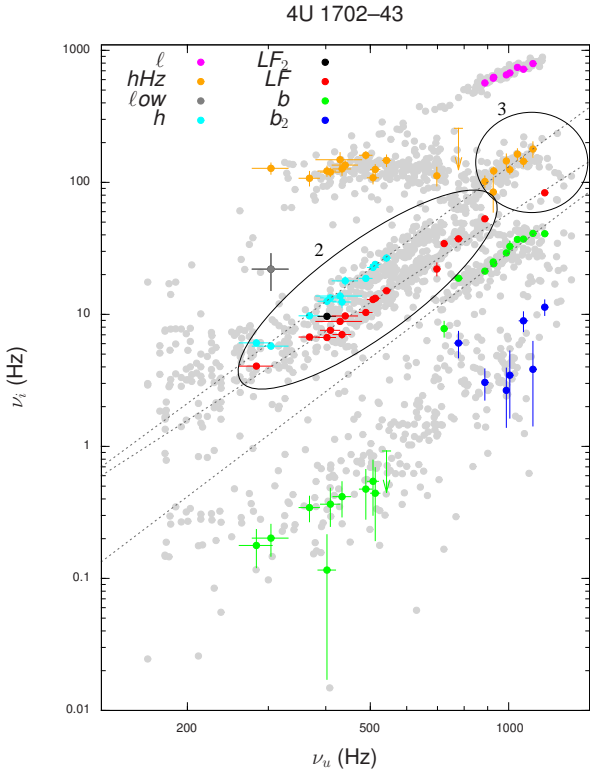


Figure C8. Same as Figure C1; but for 4U 1702-43.

identification of these features insecure and atypical for the source. We omit them from our frequency-frequency correlation fitting.

C7 SAX J1750.8-2900

In SAX J1750.8-2900 signal to noise is low, so feature identifications are less secure. In 60035-01-02-01, near $\nu_u=620$ Hz, L_h and L_{LF} can only be fitted when fixing their widths (see online version of Table C2) and are then detected at 3σ each.

L_h and L_{LF} in 93432-01-03-04 with ν_u around 200 Hz are detected at $>3\sigma$. However, ν_h is offset from the $\nu_h-\nu_u$ correlations in other sources, see Figure C12. Probably, due to low signal to noise, components between L_u and L_h remain undetected and are fitted with a broader L_h , shifting the centroid frequency to a higher value. We use this ν_h in our $\nu_h-\nu_u$ fit, because we cannot compare to similar observations of this source to confirm the possible broadening of L_h .

C8 4U 1915-05

In this source we fit a power spectral feature that we can follow over a range of 600 Hz in ν_u at a frequency that systematically falls between that of L_b and L_{LF} as observed in other sources, see Figure C13. It could be a blend of L_b and L_{LF} we fit there. As would be expected from a blend, the fractional rms- ν_u relation behaves similarly to L_h (which has much higher rms, compare Figure C14 to Figure C2) in

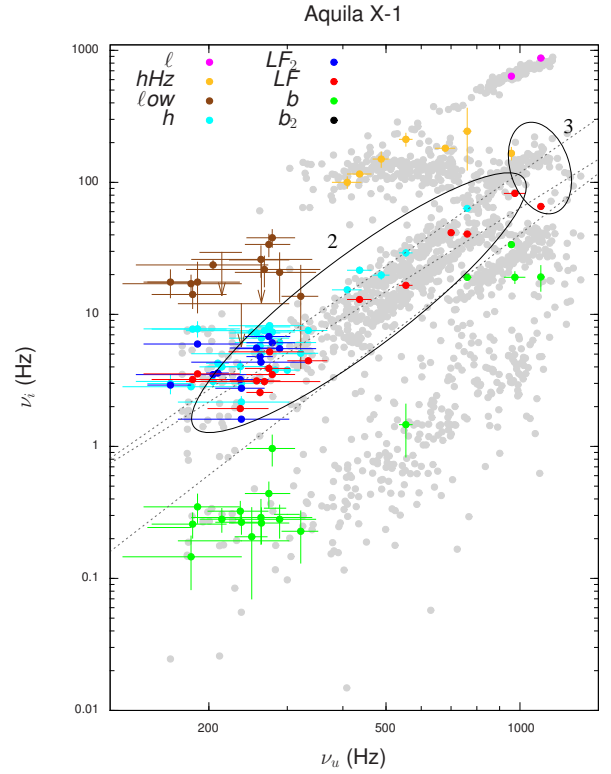


Figure C9. Same as Figure C1; but for Aquila X-1.

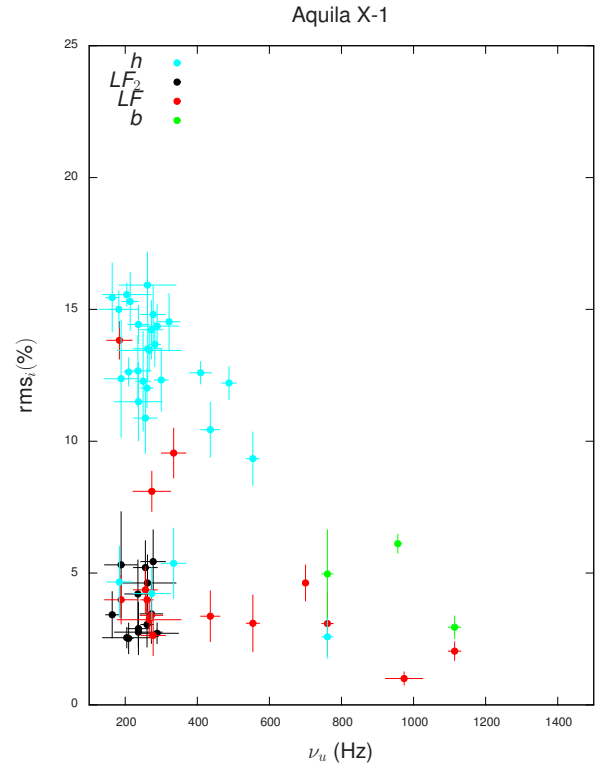


Figure C10. Same as Figure C2; but for Aquila X-1.

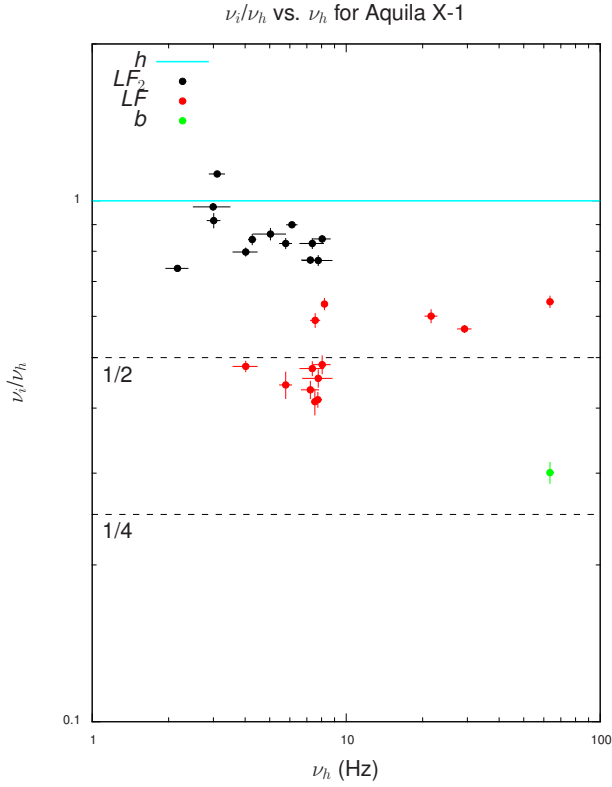


Figure C11. Same as Figure 8; for Aquila X-1.

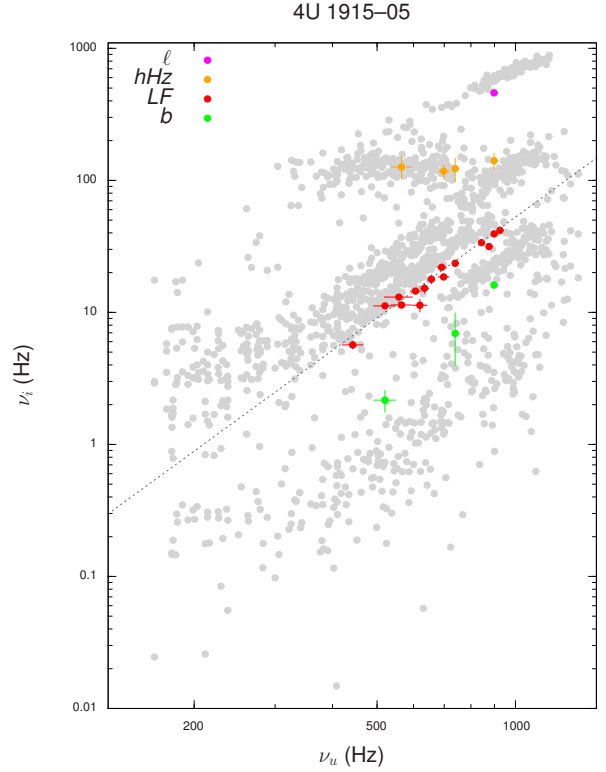


Figure C13. Same as Figure C1 but for 4U 1915-05.

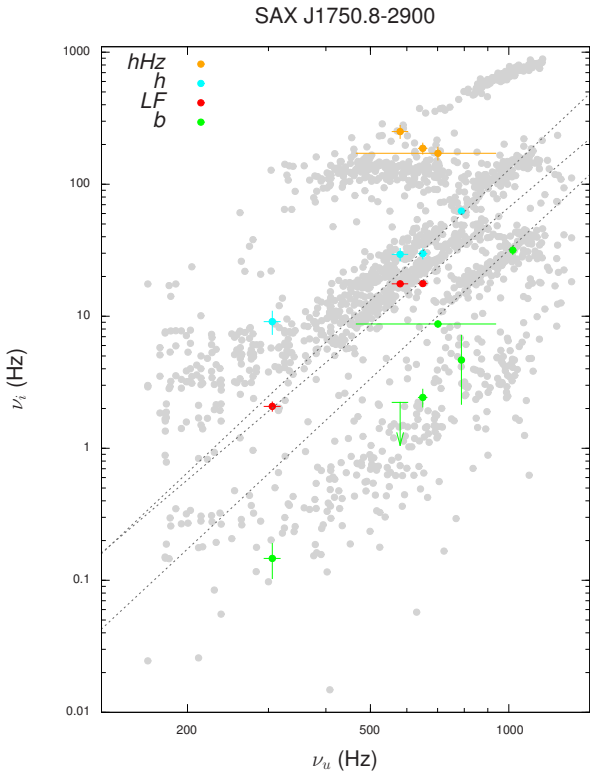


Figure C12. Same as Figure C1 but for SAX J1750.8-2900.

other sources (like 4U 1728-34). We designate this QPO as L_{LF} in Table C2 and (by plotting colour) in the figures.

C9 KS 1731-260

In this source two distinct types of power spectrum are seen where ν_u is near 200 Hz (see Figure C15): one where $\nu_{LF} \sim 0.8$ Hz, $\nu_{LF2} \sim 1.6$ Hz and $\nu_h \sim 2.5$ Hz, the other where $\nu_{LF} \sim 1.5$ Hz, $\nu_{LF2} \sim 3$ Hz, and $\nu_h \sim 4$ Hz. In terms of rms, the features in both types are similar, see Figure C16. To what extent this is related to the flattening of the correlations seen in other sources in this range is unclear.

C10 IGR J17191-2821

Similarly to SAX J1750.8-2900, in IGR J17191-2821 we can fit L_u accompanied by features at low frequency that are hard to identify due to low signal to noise. Blending could have affected these frequencies. We designate the low frequency component as L_b in Table C2 and Figure C17 (by plotting colour).

This paper has been typeset from a $\text{\TeX}/\text{\LaTeX}$ file prepared by the author.

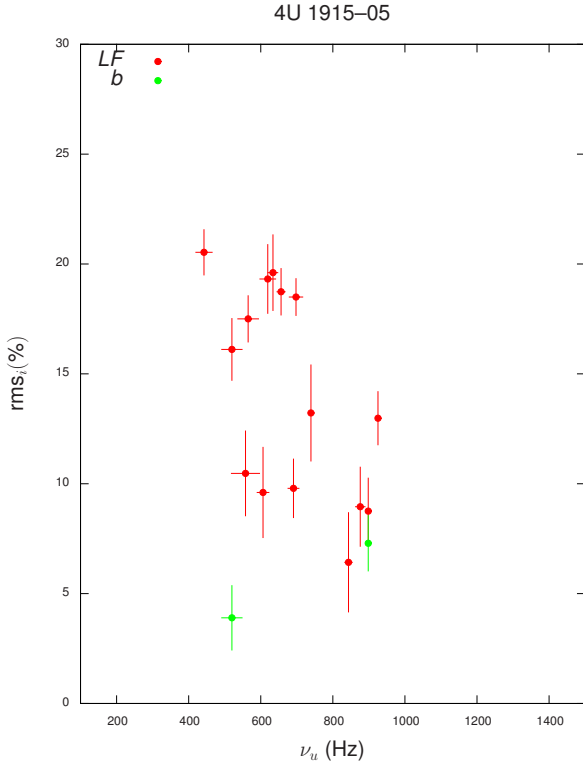


Figure C14. Same as Figure C2 but for 4U 1915-05.

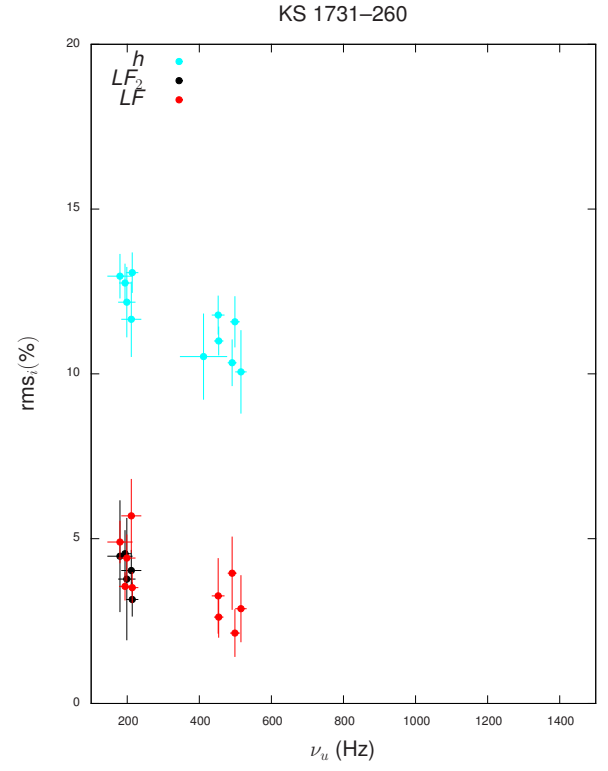


Figure C16. Same as Figure C2 but for KS 1731-260.

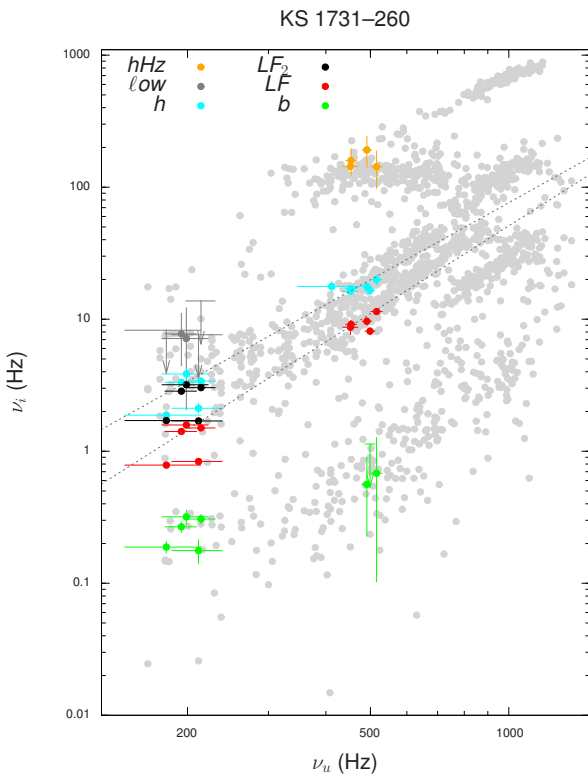


Figure C15. Same as Figure C1 but for KS 1731-260.

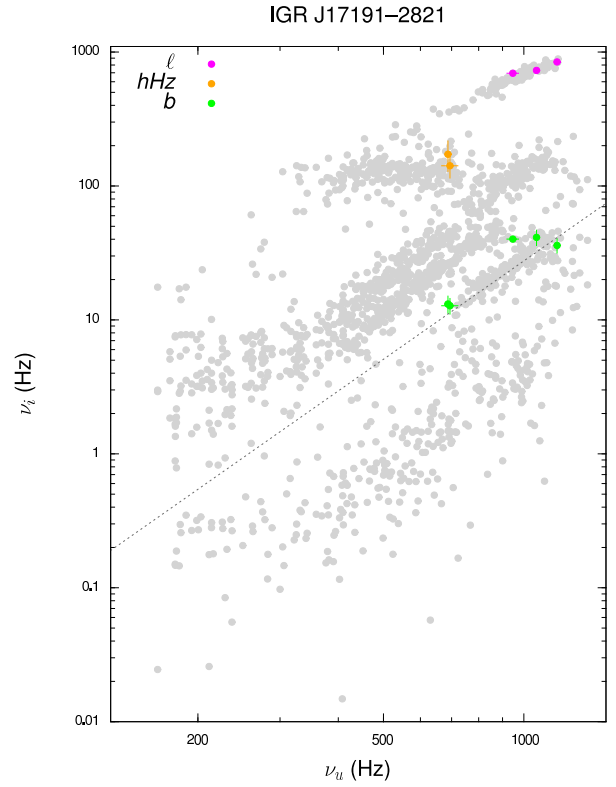


Figure C17. Same as Figure C1 but for IGR J17191-2821.